1   # A High-throughput Neurohistological Pipeline for Brain-Wide

2   # Mesoscale Connectivity Mapping of the Common Marmoset

3   Meng Kuan Lin[1], Yeonsook Shin Takahashi[1], Bing-Xing Huo[1], Mitsutoshi Hanada[1], Jaimi Nagashima[1],

4   Junichi Hata[1], Alexander S. Tolpygo[2], Keerthi Ram[3], Brian Lee[4], Michael Miller[4], Marcello G.P. Rosa[5,6],

5   Erika Sasaki[7], Atsushi Iriki[8], Hideyuki Okano[1,9], Partha P. Mitra[1,2,5]

6

7   1.   Laboratory for Marmoset Neural Architecture, RIKEN Center for Brain Science, Japan.

8   2.   Cold Spring Harbor Laboratory, Cold Spring Harbor, United States.

9   3.   Indian Institute of Technologies Madras, India.

10 4.   Center for Imaging Science, Johns Hopkins University, United States.

11 5.   Department of Physiology and Biomedicine Discovery Institute, Monash University, Australia.

12 6.   Australian Research Council Centre of Excellence for Integrative Brain Function

13 7.   Central Institute for Experimental Animals, Japan.

14 8.   Laboratory for Symbolic Cognitive Development, RIKEN Center for Brain Science, Japan.

15 9.   Department of Physiology, Keio University School of Medicine, Japan.

Abstract

Understanding the connectivity architecture of entire vertebrate brains is a fundamental but difficult task. Here we present an integrated neuro-histological pipeline as well as a grid-based tracer injection strategy for systematic mesoscale connectivity mapping in the common Marmoset (*Callithrix jacchus*). Individual brains are sectioned into ~1700 20μm sections using the tape transfer technique, permitting high quality 3D reconstruction of a series of histochemical stains (Nissl, myelin) interleaved with tracer labelled sections. Systematic in-vivo MRI of the individual animals facilitates injection placement into reference-atlas defined anatomical compartments. Further, combining the resulting 3D volumes, containing informative cytoarchitectonic markers, with *in-vivo* and *ex-vivo* MRI, and using an integrated computational pipeline, we are able to accurately map individual brains into a common reference atlas despite the significant individual variation. This approach will facilitate the systematic assembly of a mesoscale connectivity matrix together with unprecedented 3D reconstructions of brain-wide projection patterns in a primate brain.

Keywords

high-throughput pipeline; mesoscale; marmoset; tape-transfer method; registration; annotation

Introduction

The connectional architecture of the brain underlies all the nervous system functions, yet our knowledge of detailed brain neural connectivity falls largely behind genomics and behavioral studies in humans and in model research species such as rodents (Bohland et al., 2009). To fill this critical gap, a coherent approach for the mapping of whole-brain neural circuits at the mesoscale using standardized methodology was proposed in 2009 (Bohland et al., 2009). Since then, several systematic brain connectivity mapping projects for the mouse have been initialized and established, including the Mouse Brain Architecture Project (Pinskiy et al., 2015) (www.brainarchitecture.org), the Allen Mouse Brain Connectivity Atlas (Oh et al., 2014) (connectivity.brain-map.org), and the Mouse Connectome Project (www.mouseconnectome.org) (Zingg et al. (2014)). Non-human primates (NHPs) were also proposed as an important group in which to study whole-brain neural architecture. However, the high-throughput experimental approaches for mouse do not automatically apply to NHPs due to bioethical as well as experimental considerations, larger brain sizes coupled with stringent limitations on the numbers, as well as limitations arising from the increased individual variability of the brains.

There has been an increase in the usage of the common marmoset (*Callithrix jacchus*) as a model organism in contemporary neuroscience research (Belmonte et al., 2015; Kishi, Sato, Sasaki, & Okano, 2014; Miller et al., 2016; Okano & Kishi, 2018; Okano et al., 2015) (Figure 1-figure supplement 1). Marmosets offer a number of experimental advantages over the macqaue, including lower cost, ease of handling and breeding (Kishi

60   et al., 2014; Okano & Mitra, 2015), smaller brain sizes (≈35mm*25mm*20mm) that

61   potentially allow more comprehensive analysis of the neuronal circuitry, and importantly

62   the development of transgenic marmosets and the application of modern molecular tools

63   (Park et al., 2016; Sasaki, 2009; Sato et al., 2016).

64

65   Marmosets are New World monkeys, in contrast with the Old World Macaque monkeys

66   which are the pre-eminent NHP models used in basic and pre-clinical neuroscience

67   research. As depicted in Figure 1a, New World monkeys, together with Old World

68   monkeys, apes and humans, form the simian primates (order Primates, infraorder

69   Simiiformes). Simians diverged from prosimians such as lemurs and lorises

70   approximately 85 million years ago (Mya). Among the simians, New World monkeys

71   have evolved in isolation from Old World monkeys, apes and humans for at least 40

72   million years. Prima facie this seems to indicate a relative weakness in using Marmosets

73   as NHP models in contrast with the Macaques. Nevertheless, a good case can be made for

74   Marmosets as NHP models of humans, despite the earlier evolutionary divergence.

75

76   Marmosets exhibit more developed social behavior (Miller et al., 2016) and vocal

77   communication (Marx, 2016) traits, thus social-vocal Human traits (and corresponding

78   dysfunctions) might be better modeled in Marmosets than in Macaques. Marmoset brains

79   are smaller than Macaque brains and are comparable in size to some rodents (cf. Squirrels

80   and Capybara, both species of rodents, have brain volumes comparable to Marmosets and

81   Macaques). However Marmosets are phylogenetically closer to Humans than Rodents,

82   and thus have more commonality in terms of brain architecture (proportionately larger

83 and more differentiated higher order cortical areas, as opposed to primary cortical areas

84 (L. Krubitzer & Dooley, 2013) (Figure.1).

85
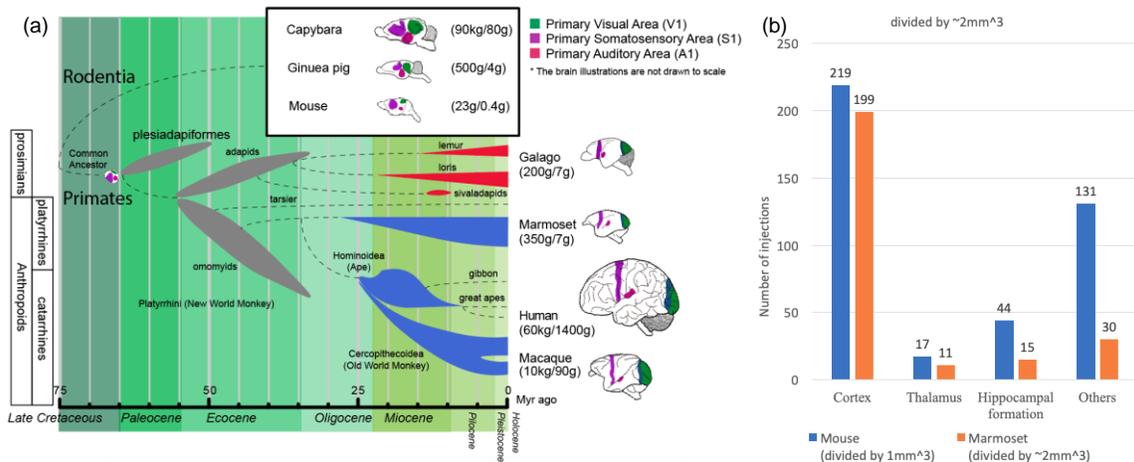
86

87 Figure 1. (a) Phylogenetic tree (Benton, Donoghue, & Asher, 2009; dos Reis, Donoghue, & Yang, 2014; dos Reis et al.,

88 2012; Janečka et al., 2007; Leary et al., 2013; Mitchell & Leopold, 2015; Springer, Meredith, Janecka, & Murphy, 2011;

89 Wilkinson et al., 2011) showing the ancestral history of extinct and extant primates, after divergence from the common

90 ancestor with rodents (top right inset box) *ca.* 75 million years (Myr) ago. The bottom bar shows geological eras.

91 Thickness of spindle shaped areas in the evolutionary tree indicate of prosperity (estimated population and numbers of

92 species) of the group along the history in extinct (gray) prosimian (red) and simian (blue) primates. Each bifurcation

93 represents the species divergence, although the divergence time typically has a wide range and remains controversial.

94 Primates diverged into platyrrhini, the New World Monkey, and catarrini, around 38.9-56.5 million years ago. Catarrini

95 further evolved into Ape, including humans, and Old World Monkey as well as macaque monkeys 25.1-37.7 million years

96 ago. Sketches of the brain in each species are shown on the right, next to their species name. The colored areas in the

97 various brain illustrations indicate the primary visual area as green, somatosensory as purple, and auditory areas as red;

98 each represents an extant primate (bottom right row) and rodent (top inset box) species' body weight (first numbers in

99 brackets) and brain weight (last numbers in brackets) sizes (Buckner & Krienen, 2013; Dooley & Krubitzer, 2013; L. A.

100 Krubitzer & Seelke, 2012). Phylogenetic tree adapted from Masanaru Takai (Takai, 2002). (b) Fractional brain region

101 volumes, and numbers of injection sites used in grid- based injection plans for marmoset (Woodward et al., 2017) and

102 mouse (Allen Institute for Brain Science, 2017). Bar plots show the number of grid-injection sites within the displayed

103 compartment in each species, assuming a spacing between injection sites of ~1 mm isometric in mice, and ~2-3 mm

104 isometric in marmosets.

105

106 Following the BRAIN (Brain Research through Advancing Innovative Neurotechnologies)

107 Initiative in the U.S. and the HBP (Human Brain Project) in Europe in 2013, Japan

108 launched the Brain/MINDS project (Brain Mapping by Integrated Neurotechnologies of

109 Disease Studies) with a focus on the common marmoset (*Callithrix jacchus*) as an NHP

110 model (Okano & Mitra, 2015) (http://www.brainminds.jp/). As part of Brain/MINDS, a

111 combined histological/computational pipeline was established at RIKEN to develop a

112 mesoscopic whole-brain connectivity map in the Marmoset. The corresponding

113 methodology is described in this manuscript.

114

115 Tract-tracing methods remain the gold standard for studying neural circuit structure at the

116 whole brain level (Bakker, Wachtler, & Diesmann, 2012). Previous brain-wide

117 connectivity mapping for non-human primates have been based on literature curation and

118 meta-analyses. A pioneering survey by Felleman & Van Essen (1991) reviewed 52

119 studies, including both anterograde and retrograde tracing results, to generate a

120 connectivity matrix of 33 brain regions in the visual system of macaque monkeys (Table

121 1). Building upon Felleman & Van Essen (1991) , a more comprehensive database of

122 macaque brain connectivity, CoCoMac (Collation of Connectivity data on the Macaque

123 brain, cocomac.g-node.org) (Bakker et al., 2012; Kötter, 2004; Klass E. Stephan et al.,

124 2001), surveyed over 400 tracing studies with ~3,300 injections and established a

125 connectivity matrix of 58 brain regions (Modha & Singh, 2010; Klaas Enno Stephan,

126 2013) (Table 1). While the historical tracing studies mostly contain qualitative

127 information, more recent studies have aimed at building a quantitative connectivity

128 database of the macaque brain (Falchier, Clavagnier, Barone, & Kennedy, 2002; Markov

129 et al., 2014; Markov et al., 2011) (core-nets.org; Table 1).

	Data	Species	Injections	anterograde tracer	retrograde tracer	Connectivity matrix	Source
Journal papers	no whole-brain image data	Macaque	370	153	217	33x33	Felleman & Van Essen 1991 (52 studies)
			3279	1429	1873	58x58	CoCoMac (459 studies)
			39	0	39	29x91	Markov et al. 2014
		Marmoset	428	93	395	-	35 studies (Bibliography in supplement)
Whole-brain image data	Nissl images overlaid with cell locations (Rosa Lab data set)	Marmoset	140	0	140	-	Online
	This paper: Whole-brain set of cross-modal serial sections (Nissl,Myelin, IHC, Fluoro) + MRI		188	94	94	-	This paper

Table 1. Past and present summary of historical tract-tracing studies in macaque and marmoset monkeys. Three resources of macaque monkey brain connectivity are shown. Felleman & Van Essen (Felleman & Essen, 1991) and CoCoMac each surveyed a set of studies to generate the connectivity matrix (full reference list in Supplementary File 2). Note that CoCoMac is inclusive of the work collected in Felleman & Van Essen (Felleman & Essen, 1991). Around 235 injections lack tracer direction information. Markov et al. 2014 (Markov et al., 2014) was a single study using only the retrograde tracer to generate the connectivity matrix as well as quantifying the connection strengths. We have surveyed 35 marmoset brain tracing studies that contain 428 tracer injections including both anterograde and retrograde tracers. A complete connectivity matrix is not yet available for the marmoset brain. To date, the most comprehensive marmoset brain connectivity resource available online (http://monash.marmoset.brainarchitecture.org) includes 140 retrograde tracing studies. As part of the current pipeline, we have placed over 188 tracer injections including both anterograde and retrograde tracers. For both macaque and marmoset brain injections, bidirectional tracer injections were double counted as one anterograde and one retrograde tracer injection.

For the Marmoset, an online database of >140 retrograde tracer injection studies in about 40 brain regions is available online (http://monash.marmoset.brainarchitecture.org) (Piotr et al., 2016). By surveying 35 tract tracing studies (Supplementary File 2) in marmosets since the 1970s, we have collected data from over 400 injections, but much of this knowledge cannot be easily integrated with current efforts given the use of older nomenclatures, and the lack of access to primary data. A full connectivity matrix is yet to be established (Table 1). Nevertheless existing knowledge about the marmoset visual,

151   auditory, and motor systems indicate strong similarities between marmoset and macaque

152   brain circuitry, suggesting a preserved brain connectivity plan across primates (Bakola,

153   Burman, & Rosa, 2015; de la Mothe, Blumell, Kajikawa, & Hackett, 2012; Solomon &

154   Rosa, 2014). Comparing two NHP brain architectures (Marmoset, Macaque) will help to

155   better contextualize Human brain circuit architecture.

156

157   None of these earlier studies in NHPs have used a single, consistent methodology

158   employing a unified experimental-computational workflow, dedicated to systematic

159   mesoscale connectivity mapping. In addition, an automated throughput image analysis is

160   required for the whole-brain circuit reconstruction and mapping (Hua, Laserstein, &

161   Helmstaedter, 2015). This became the goal of the pipeline described in this paper.

162   Importantly, brain-wide data sets are already available for grid-based tracer mapping

163   projects in the Mouse. A corresponding data set generated using similar techniques will

164   allow us to gain a more unified view of primate brain connectivity architecture, and also

165   permit an unprecedented comparative analysis of mesoscale connectivity in Rodents and

166   Primates.

167

168   **The injection-grid approach to whole-brain mesoscale connectivity mapping**

169

170   Mapping the brain-wide neural circuitry in large vertebrate brains remains one of the

171   most important tasks in neuroscience, yet raises tremendous practical and theoretical

172   challenges. The ideal data set would contain the position, morphology, synaptic

173   connectivity together with transmitter/receptor identities at each synapse, and also spatial

maps of the diffuse neuromodulatory transmitters and receptors of every neuron. This is clearly not achievable in practical terms. For example, EM based mapping of individual synaptic connectivity and morphology of every neuron remains impractical for a brain as large as the Marmoset.

Even if comprehensive mapping was performed in one brain, there would remain the problem of individual variation across brains, which would ideally require doing the same detailed map for many brains. All current approaches to this problem therefore constitute practical compromises (e.g. EM mapping of synaptic connectivity for larger vertebrate brains is currently confined to small brain regions). The grid-injection based approach achieves brain-wide coverage but sacrifices the detailed synaptic connectivity, revealing a species-specific, coarse-grained circuit architecture. The availability of 3D volumetric data sets at light microscopic resolution, with the possibility of quantitative analysis and across-brain comparisons, sets this approach apart from classical neuroanatomical studies which are more targeted (e.g. to individual brain regions for injection placement, possibly to test specific hypotheses) and have largely been carried out in the era before digitizing whole brains was practical.

Within the broad approach, some questions need to be addressed: treatment of individual variation across brains, relation to classical neuroanatomical approaches based on atlas-parcellations, and technical sources of variation, being the difficulty in controlling the locations and sizes of injections, and most importantly the total number of injections. We briefly comment on these inter-related considerations here as they pertain to the design of our injection grid-plan. In the later discussion section, we present some analysis of the

198   degree of individual variation in the data set gathered for this project, and considerations

199   related to completing whole-brain coverage. Further information may be found in

200   Appendix 9 and 10.

201

202   ***Planning the grid*.** Classical neuroanatomical reference atlases list hundreds of individual

203   gray-matter regions or cell groups (including cortical regions and subcortical nuclei),

204   separated by more or less well-defined boundaries. Within regions, continuous gradients

205   may be present. These atlases were developed largely based on the spatial distributions of

206   morphologies and chemo-architectures of the neuronal somata, and to a lesser extent on

207   the connection architecture. As new information becomes available from modern

208   techniques, these atlases are likely to change, also the atlases do not provide *prima facie*

209   information about individual variation, as they are based on an individual brain (or more

210   recently on averages across brains). It is important to take into account the accumulated

211   knowledge represented by these atlases in planning a grid; on the other hand, the atlases

212   themselves represent imperfect knowledge, and sampling brain-space on a regular grid

213   could itself reveal the necessary meso-architecture.

214

215   We adopt a compromise, by starting from a roughly regular grid, working backwards

216   from the total number of injections that can realistically be placed/processed within a

217   practical time frame (of several years) and within the constraint of the availability of

218   experimental animals. We therefore started with a grid spacing of ~2mm, but then

219   adapted the grid in the following ways: (i) grid points overlapping with atlas boundaries

220   were moved to be closer to compartment centers; (ii) atlas compartments smaller than 8

221   mm^3 were assigned injections upto a size cutoff. Placing this size cutoff at 0.27 mm^3

222   produces a total of 356 injection centers in 241 target structures in one hemisphere's grey

223   matter. In cerebral cortex, this corresponds to 221 injection centers in 118 target

224   structures, comprising 74% of the total grey matter volume. Details are presented in

225   Appendix 9.

226

227   We inject each site with an anterograde and a retrograde tracer (in separate animals). To

228   maximize utilization of animals we place 4 injections/animal, 2 anterograde and 2

229   retrograde. Our approach is conservative: better availability and utilization of colors in

230   the tracers could permit more injections per animal. Notably, we are able to process

231   significantly more injections per animal than is possible with single-color 2-photon light

232   microscopy, which is important for a primate species such as the Marmoset to minimize

233   the number of animals used.

234

235   ***Individual variation.*** Classical neuroanatomical studies may place multiple injections in

236   separate animals at a single target to address biological variation. This is impractical for

237   the current approach it would require too many animals. Nevertheless, we achieve an

238   effective N=2 per long range projection when combining the results of anterograde and

239   retrograde tracing. Additionally, we tailor injections to the individual variations in

240   animals when using in-vivo MRI guidance to target specific sub-cortical nuclei and using

241   landmarks in injecting cortical sites. Finally, results from different animals are mapped

242   onto a common reference atlas using diffeomorphic mapping utilizing the

243   cytoarchitectonic contrast present in the multimodal histological data gathered in the

244   pipeline. In these ways the grid-approach addresses the issues of individual variation. An

245   analysis of brain compartment size variations across animals, as well as of the injection-

246   size variations, is presented in Appendix 10.

247 # Materials and methods

248

249   A high throughput neurohistological pipeline was established at the RIKEN Center for

250   Brain Science, based on the pipeline developed for the MBA project (Pinskiy et al., 2015)

251   at CSHL. The pipeline employed a customized tape-transfer assisted cryo-sectioning

252   technique to preserve the geometry of individual sections. Each brain was sectioned

253   serially into a successive series of four 20μm sections: a Nissl stained section, a Silver

254   (Gallyas) myelin stained section, a section stained (ABC-DAB) for the injected cholera

255   toxin subunit B (CTB) tracer and an unstained section imaged using epifluorescence

256   microscopy to visualize the results of fluorescent tracer injections. Three types of

257   fluorescent neural tracers were injected into the brain to reveal the mesoscale neural

258   connectivity. The four sets of sections: Nissl, myelin, CTB and fluorescent sections were

259   processed and imaged separately, and later re-assembled computationally. A

260   computational pipeline was established to perform high-throughput image processing. A

261   common reference atlas (Hashikawa, Nakatomi, & Iriki, 2015; Paxinos, Watson, Petrides,

262   Rosa, & Tokuno, 2012) was registered to each individually reconstructed brain series and

263   the projection strengths were suitably quantified.

264

265   **2.1 Experimental pipeline**

266

267   All experimental procedures were approved by the Institutional Animal Care and Use

268   Committee at RIKEN and a field work license from Monash University, and conducted in

269   accordance with the Guidelines for Conducting Animal Experiments at RIKEN Center

270   for Brain Science and the Australian Code of Practice for the Care and Use of Animals

271   for Scientific Purposes. Female marmosets (*Callithrix jacchus*), 4 to 8 years old, 330g -

272   440g in weight, were acquired from the Japanese Central Institute for Experimental

273   Animals.

274

275   ***In-vivo* MRI**. Upon habituation, the marmosets promptly went through magnetic

276   resonance (MR) imaging. MR scans were performed using a 9.4T BioSpec 94/30 US/R

277   MRI scanner (Bruker, Biospin, Ettlingen, Germany) with actively shielded gradients that

278   had a maximum strength of 660 mT/m. Several MRI protocols were carried out for each

279   individual marmoset. T1 mapping and T2-weighted images (T2WI) were used in *in-vivo*

280   MR imaging. More details of the scan protocol can be found in Appendix 1.

281

282   **Neuronal tracer injections.** To conserve animals, four tracers were placed in the right

283   hemisphere of each marmoset, including two anterograde tracers: AAV-TRE3-tdTomato

284   (AAV-tdTOM) and AAV-TRE3-Clover (AAV-GFP), and two retrograde tracers: Fast

285   Blue (FB) and CTB. Surgical procedures for tracer injections were adapted from the

286   previously established protocols(Reser, Burman, Richardson, Spitzer, & Rosa, 2009;

287   Reser et al., 2013; Reser et al., 2017). Tracers were delivered at the injection sites using

288   Nanoject II (Drummond, USA), with dosage controlled by Micro4 (WPI, USA). For

289   cortical injections, each tracer was delivered with depths of 1200μm, 800μm, and 400μm

290   sequentially perpendicular to the cortical sheet, with equal volumes. The planning for

291   tracer injections approximately followed a uniform 2 x 2 x 2mm grid spacing, intended to

292   cover the entire brain cortical and subcortical regions (Grange & Mitra, 2011) (Appendix

293   2). The current data set used to validate the method presented here includes 118

294   injections. At each injection site, one retrograde and one anterograde tracer was injected

295   separately to cover the efferent and afferent projections of that site. Figure 2a,b shows

296   currently covered injection sites.

297

298   ***Ex-vivo*** **MRI and cryo-sectioning**. After tracer injection and a 4-week incubation period,

299   the marmoset brain was perfused with a 0.1M phosphate buffer (PB) flush solution

300   followed by 4% paraformaldehyde (PFA) in 0.1M PB fixation solution. The same MR

301   scan protocol for *in-vivo* MRI was used for *ex-vivo* Diffusion Tensor Imaging (DTI)

302   scanning. Additional high-resolution (300μm) T2-weighted images (T2WI) were carried

303   out for *ex-vivo* MR imaging (Appendix 1). Following fixation, the brain was transferred

304   to 0.1M PB to take an *ex-vivo* MRI. It was then immersed in 10% then 30% sucrose

305   solution over a 48-hour period to safeguard against thermal damage. The brain was

306   embedded in freezing agent (Neg-50^{TM}, Thermo Scientific 6505 Richard-Allan Scientific)

307   using a custom developed apparatus and a negative cast mold of the brain profile. The

308   apparatus was submerged in an optimal cutting temperature compound to expedite the

309   freezing process (Pinskiy et al., 2013). More details can be found in Appendix 3.

310

311   Cryo-sectioning of the brain was performed using a Leica CM3050 S Cryostat in a

312   humidity chamber set at 18°C and 80% humidity. The cryostat specimen temperature

313   was set to -15 to -17°C while the chamber temperature was set to -24°C. This temperature

314   differential was used to make certain the tissue was never in danger of being heated

315   unnecessarily. Brains were cryo-sectioned coronally on a custom made cryostat stage

316   using the tape transfer and UV exposure method (Pinskiy et al., 2015) (Appendix 4).

317   Every four consecutive sections were separately transferred to four adjacent slides, to

318   establish the four series of brain sections to be stained for different methods. Each section

319   was 20μm in thickness, hence the spacing between every two consecutive sections in the

320   same series was 80μm. The four slides were transferred and cured for 12 seconds in a

321   UV-LED station within the cryostat. All cured slides were placed inside a 4°C

322   refrigerator for 24 hours to allow thermal equilibration.

323

324   **Histological staining**. Separate histological staining processes were performed on the

325   different series of brain sections (Appendix 5). High-throughput Nissl staining of neuron

326   somata was performed in an automated staining machine (Sakura Tissue-Tek Prisma,

327   DRS-Prisma-J0S) (Figure 2c). The myelin staining technique used a modified

328   ammoniacal silver stain originally developed by Gallyas (Gallyas, 1979). The present

329   modification provided higher resolution of fiber details that could be used for

330   myeloarchitecture identification. A representative magnified image of myelin staining in

331   the V4 (middle temporal crescent) visual cortex is shown in Figure 2d. Using a modified

332   protocol developed for the MBA project at CSHL, the staining of retrograde and

333   anterograde CTB label was successfully attained (Costa et al., 2000) (Figure 2e). Finally,

334   retrograde fluorescent tracers revealed originating somata while the anterograde tracers

335   revealed projecting axons from fluorescent imaging. Figure 2(f-h) shows the

336   simultaneous fluorescent tract tracing using AAV-GFP, AAV-tdTOM and FB within the

337   same brain. More detailed high-magnification images can be found in Figure 2-figure

338   supplement 2.

340

341

342

343
344
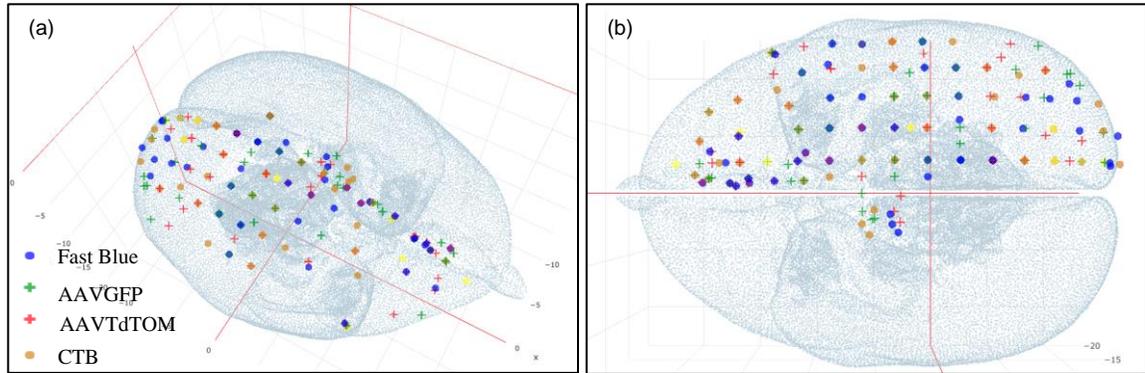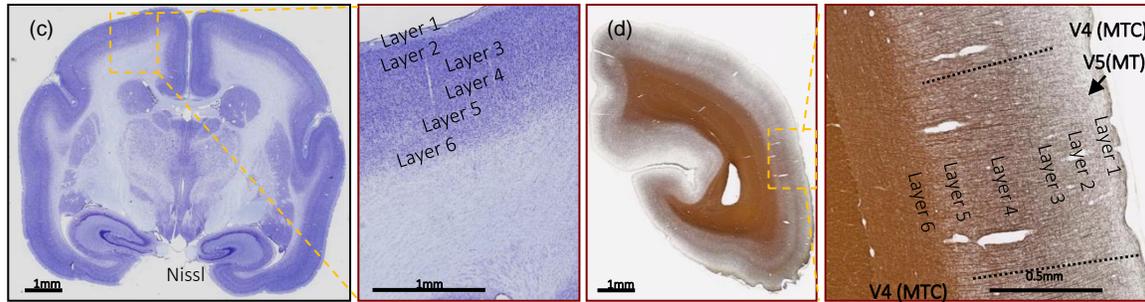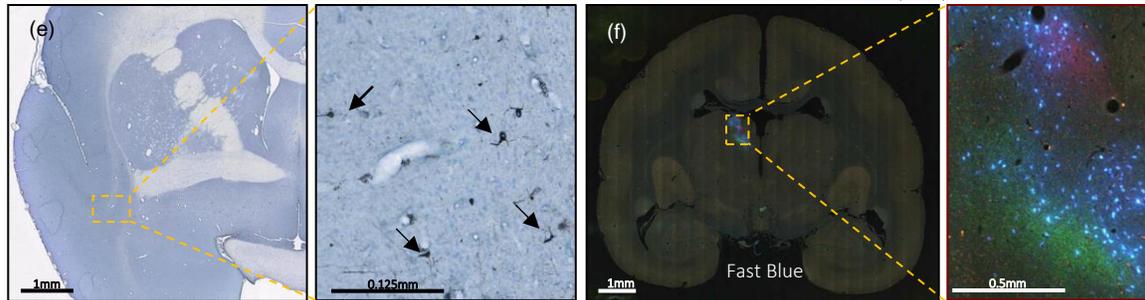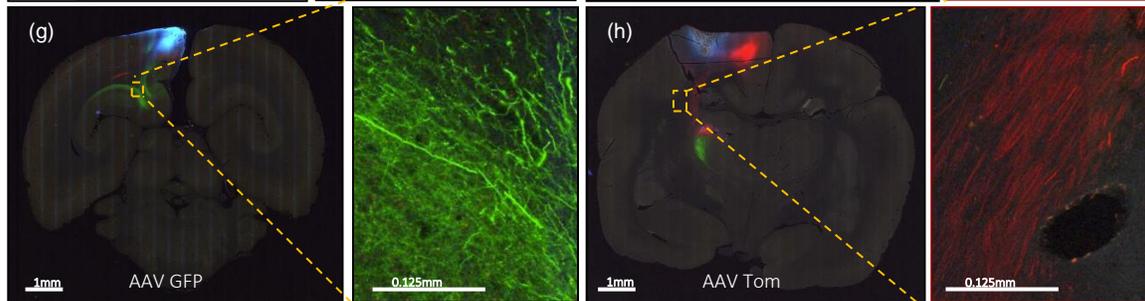
345 Figure 2. (a, b) Current successful injection sites using 2 x 2 x 2mm grid spacing in the marmoset cortex in (a) 3D and (b)

346 2D dorsal view, in stereotaxic coordinates (Paxinos et al., 2012). (b) Current successful injection sites. Each tracer is

347 represented with a different color of marker: blue: Fast Blue; green: AAV-GFP; red: AAV-tdTOM; brown: CTB. Two tracers,

348 one anterograde and one retrograde, are injected at each site. (c-h) Sample coronal brain section images of four series. (c)

349 A coronal section after Nissl staining is shown with increasing magnification. Around Area 3a (magnification box), 6

350 cortical layers and the white matter are clearly differentiable based on cell body density. (d) A coronal section of the left

351 hemisphere after silver staining showing myelin. Around Visual area V4T (Middle Temporal) crescent; magnification box),

352 layers I-VI can be clearly characterized based on the myelin fiber density. Heavy myelination can be seen in layer 3 and

353 continues into layer 4-6 with clear inner and outer bands of Baillarger. (e) Partial coronal section after

354 immunohistochemistry treatment for CTB. After injection into Area 10, CTB labeled neurons were found in the claustrum

355 (magnification box). The arrows indicate CTB- labeled cells at 0.125mm. (f-h) Coronal sections in different parts of the

356 brain showing fluorescent tracers including (f) retrograde tracer Fast Blue (g) anterograde tracer AAV-GFP, and (h)

357 anterograde tracer AAV-tdTOM.

358

359 The pipeline adopted the Sakura Tissue-Tek Prisma system for high-throughput staining

360 purposes. Upon completion of auto staining, the system loaded the dehydrated slides into

361 an automatic coverslipper (Sakura Tissue-Tek Glas, GLAS-g2-S0) where 24x60mm

362 cover glass (Matsunami, CP24601) were applied with DPX mounting media (Sigma,

363 06522); then put into drying racks for 24 hours. Figure 3 shows the overall steps as well

364 as time taken to process one marmoset brain before moving to the computational pipeline

365 starting with imaging.

366
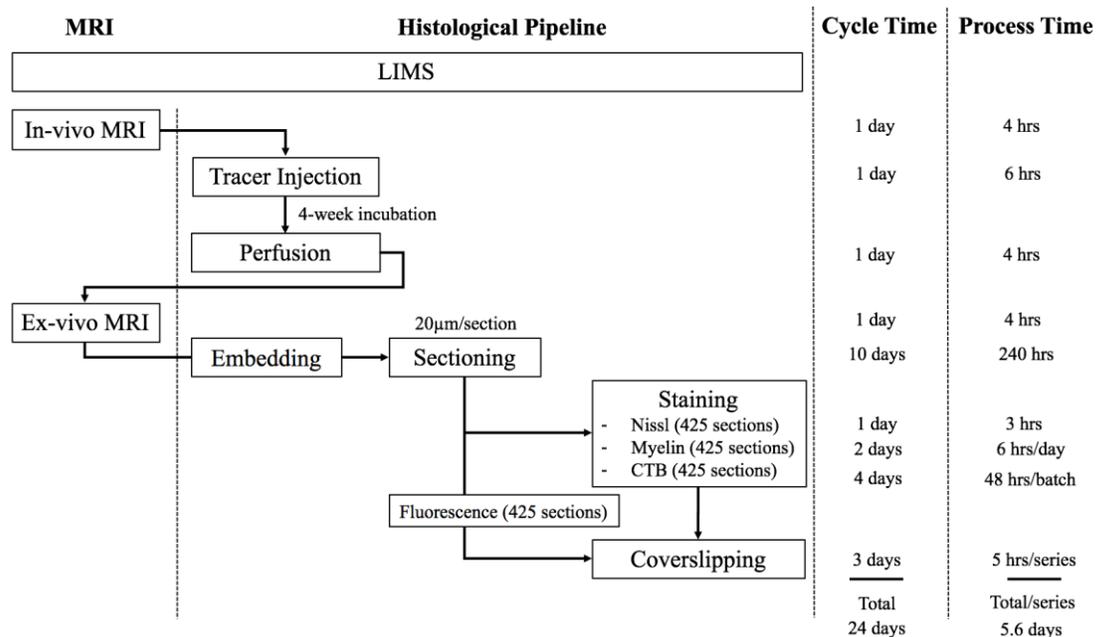
367

368 Figure 3. The workflow of the experimental pipeline and the processing time for one marmoset brain. Arrows show the

369 sequence of individual experiments. A custom-made LIMS (Laboratory Information Management System) performs

370 housekeeping for the entire process and constitutes an electronic laboratory notebook. The entire brain is sectioned into

371 ~1700 sections, ~ 400 in each series. Each series include ~295 slides, comprising of 1/3 of the slides with 2 brain

372 sections mounted and 2/3 with 1 brain section/slide. Coverslipping includes the drying and clearing stages. The

373 processing time does not include the overnight waiting period after sectioning in each batch. The overnight incubation

374 time is excluded in the CTB procedure as well as the overnight dehydration in a myelin stain. Processing Time on the

375 right shows the time involved in processing each experimental step, in hours. The Cycle Time (in days) shows the total

376 time required to initiate and finish the entire procedure from start to finish, including quiescent periods, before

377 commencing the procedure for another brain. Total time on the bottom is not a summation of the individual procedure

378 times above because of parallel, pipelined processing which reduces total processing times. For example, when Nissl

379 series are being processed in the automatic tissue staining machine for Nissls, CTB and myelin staining can be performed

380 simultaneously at other workstations.

381

382 Including imaging, one full Nissl brain series can be completed in 6 days. The myelin

383 series including imaging requires 6.4 days using a limited 60-slide staining rack. The

384 CTB series took a total of 7.9 days to complete due to batch limitations (3.5 batches with

385 120 slides/batch in total). The time for completion for the fluorescent brain series was 8

386 days; the slide scanning time on the Nanozoomer used in the project is approximately

387 twice the brightfield scanning time. Overall, the four separate series of one brain could

388 completed in two weeks (a pipeline processing rate can be found in Appendix 8). The

389 digitized brains are then passed onto the computational pipeline including atlas

390 registration, cell and process detection and online presentation.

391

392 **2.2 Computational pipeline**

393

394 All the prepared slides were scanned by series with a Nanozoomer 2.0 HT (Hamamatsu,

395 Japan) using a 20x objective (0.46 μm/pixel in plane) at 12-bit depth and saved in an

396 uncompressed RAW format. Nissl, myelin and CTB series were brightfield scanned.

397 Fluorescence series were scanned using a tri-pass filter cube (FITC/TX-RED/DAPI) to

398   acquire the 3 RGB color channels for each slide. A Lumen Dynamics X-Cite *exacte* light

399   source was used to produce the excitation fluorescence.

400

401   The RAW images for all four series of slides comprise ~9 terabytes of data for each brain.

402   In order to process these large data volumes, the pipeline includes networked

403   workstations for data-acquisition, image processing and web presentations. All systems

404   were connected to two directly attached data storage nodes to ensure that all data were

405   continuously saved and backed up. All components were integrated with 10 Gigabit

406   Ethernet (10G network) to provide a cohesive solution (Appendix 6). The average node-

407   to-node transfer rate was on the order of 250-450 MB/s, including limitations of hard disk

408   speed.

409

410   Imaging data were collected from the Nanozoomer and then automatically transferred to

411   a data acquisition system. This step ensured uninterrupted scanning regardless of the

412   limited disk space on the Nanozoomer system relative to the amount of data being

413   acquired. The data acquisition system is the central repository for image pre-processing

414   including image cropping, conversion, compression (Appendix 7).

415

416   The quality control (QC) service was applied to all stages of experimentation and image

417   data flow in order to correct and improve the pipeline process organically. The

418   experimental pipeline process information was recorded in an internal Laboratory

419   Information Management System (LIMS). It supported the workflow by recording the

420   detailed status of each experimental stage for each brain. Similarly, a separate online QC

421   portal dictated all the image pre-processing stages (Figure 4). Through the LIMS and QC

422   portal, it was possible to flag damaged sections to avoid unnecessary post-processing and

423   identified the need to repeat a specific processing stage.

424
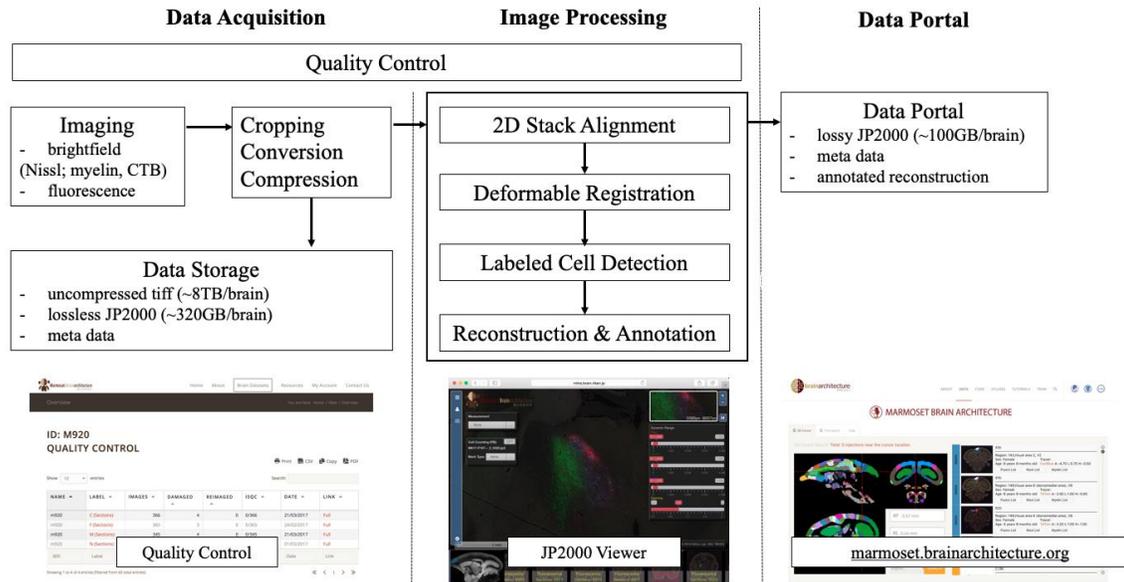
425

426   Figure 4. A flow chart showing the workflow of the computational pipeline, from data acquisition to image processing and

427   finally dissemination on the public data portal. Arrows show the data flow. A Quality control system is implemented at

428   every stage of the pipeline until final data release. The display of the data portals is to allow interactive service. (a) Quality

429   control site (snapshots on the bottom left) which helps improve the pipelines process speed and manually flags

430   unnecessary sections to avoid further post-processing. (b) An Openlayer 3.0 JPEG2000 viewer (snapshots on the bottom

431   middle) including several controls such as dynamic range, gamma, measurement and auto cell detection tool to allow for

432   a users' interpretation (Lin et al., 2013). (c) The data portal site (snapshots on the bottom right) helps to host all

433   successful and processed dataset for publishing purposes.

434

435   Image registration, cross-modal registration and automatic annotation, and tracing signal

436   detection were performed in the image processing server. Images of individual sections

437   were downsampled by 64 times and registered to one another using rigid-body

438   transformation (William, Karl, John, Stefan, & Thomas, 2011). Registered 2D images

439   were used to create a 3D volume of the brain in NIfTI format (NIfTI-1 Data Format,

440 2016) for each series. The transformation matrix for each downsampled image was

441 applied to the corresponding full resolution image.

442

443 The brain outline of Brain/MINDs atlas (Woodward et al., 2017) was applied to the

444 downsampled images after 2D registration to separate the brain regions from background

445 and ventricles. Automatic annotation of the brain structures was achieved by registering

446 the Brain/MINDs atlas to *ex-vivo* MRI and then aligned to the 2D registered Nissl series

447 ("target images"). A 3D global affine transformation was applied to move the atlas images

448 into the coordinate space of the MRI images. After transformation, the atlas images was

449 matched to the MRI images using Large Deformation Diffeomorphic Metric Mapping

450 (LDDMM)(Ceritoglu et al., 2010) which transforms the atlas coordinate to the MRI

451 image coordinate system. The same method was applied again to the transformed atlas

452 images in order to match the target Nissl images. Individual brain regions could be

453 automatically identified based on the transformed atlas. Figure 5a shows the example of

454 automatic registration from Brain/MINDs atlas to target Nissl images. Cross-series

455 registration using Euler2DTransform from Insight Segmentation and Registration Toolkit

456 (ITK, 2017) was performed to align 64-time downsampled myelin, CTB and fluorescence

457 series of images to target Nissl images (Figure 5b-d). Finally, the transformation matrices

458 calculated from the downsampled images were applied to the corresponding full

459 resolution images. The annotations from the transformed atlas were aligned with the

460 histology images of each series.
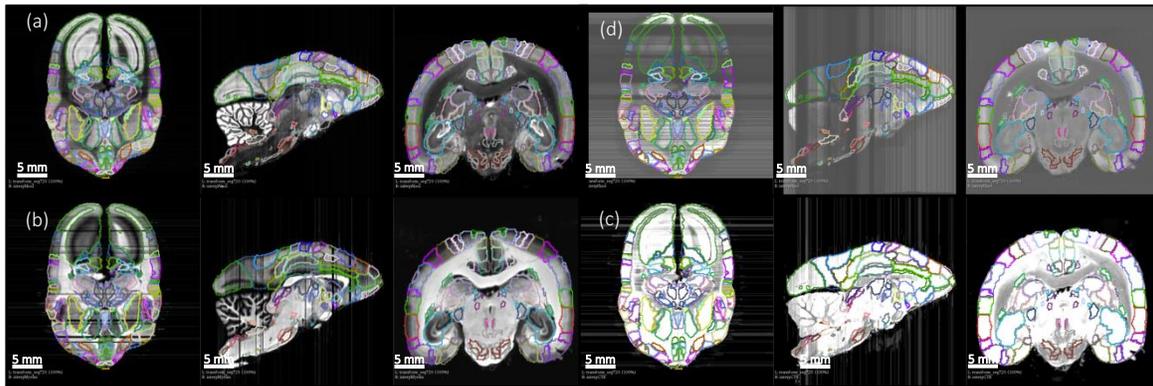
Figure 5. 3D deformable registration and atlas mapping of all four series. The Brain/MINDs atlas was registered with *ex-vivo* MRI volume, and subsequently registered to target Nissl series (a). The shaded areas indicate missing sections at the end of processing (quality control). Other series including (b) myelin, (c) CTB and (d) fluorescence series were cross-registered to target Nissl series, and aligned with the atlas annotations. Only gray scale images are shown and they are sufficient for the registration process. Sample sections in transverse (left), sagittal (middle), and coronal (right) were shown for each series.

Injection volume was estimated by measuring the tracer spread at the injection site. Automatic cell and process detection was applied to individual registered sections in order to compute a draft whole-brain connectivity matrix. As an integral part of the computational pipeline, a data portal was developed to allow for viewing and interpreting high-resolution images online (http://marmoset.brainarchitecture.org). By incorporating an Openlayer 3.0 image server with a custom image viewer, the data portal allows fully interactive zoom and pan, supports online adjustment of RGB dynamic range and contrast, as well as gamma adjustment (Figure 4). The data portal also provides visualization of cell detection results and an interactive tool for injection volume measurement.

481   **Successful re-assembly of 3D volumes**: In order to evaluate the quality of the image

482   registration pipeline, we applied computational approaches to separately register series

483   acquired for individual data modalities into separate volumes. Both high-quality and low-

484   quality section images with staining issues, image variation, or artefacts were considered

485   in the process. Adoption of the tape transfer method allowed us to maintain the geometry

486   of the brain sections in the high-quality 20μm section images. This allowed successful

487   section-to-section (2d) alignment using only rigid-body transformations. Poor-quality

488   sections such as sections with folding, tears, artefacts and discoloration missed from the

489   previous QC stage were selected by visual inspection and excluded from the 2d

490   alignment step. Less than one percent of total sections were excluded. Figure 6 (left)

491   shows one marmoset brain with different staining procedures in coronal, sagittal and

492   transverse planes after image reconstruction. It also shows the results of how the

493   geometry of the brain has been maintained in each series.

494
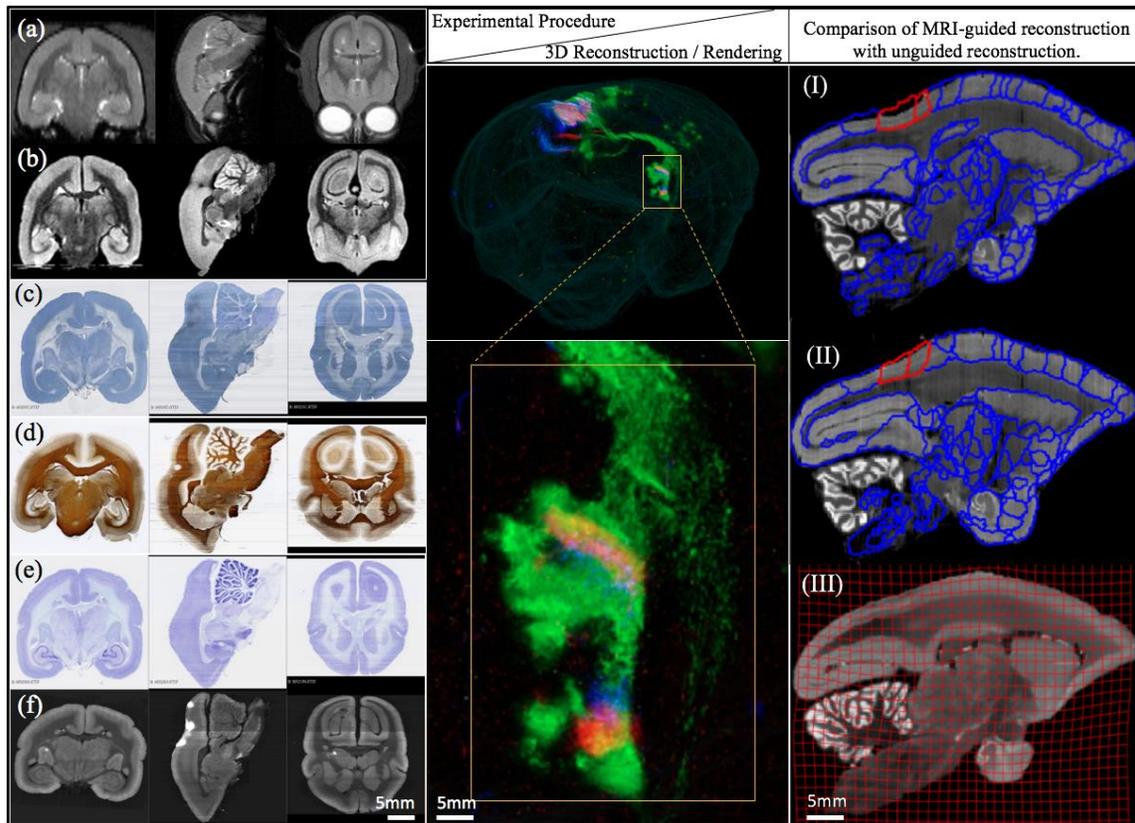
Figure 6. (left) Views of one marmoset brain after each experimental protocol: (a) *in-vivo* MRI (b) *ex-vivo* MRI (c) CTB staining (d) myelin staining (e) Nissl staining (f) fluorescence imaging. Coronal, sagittal and transverse planes at the same (MRI) or consecutive sections (staining series) are shown with 3D registration and reconstruction. (middle) A 3D visualization of the fluorescent tracer projection. Simultaneous anterograde (red, green) and retrograde (blue) tracing reveals a reciprocal connection between the dorsal medial visual area (injection site) and the thalamus (anterograde projection and retrograde cell labeled sites) especially lateral posterior nucleus and lateral pulvinar. The connectivity can be observed with this 3D visualization which shows the pathway of tracers in through the brain volume. (right) Comparison of MRI-guided reconstruction with unguided reconstruction. I: the target Nissl stack reconstruction by unguided piecewise neighbor-to-neighbor alignment. II: the MRI-guided reconstruction. III: same- subject T2-weighted MRI.

Atlas registration: Using external references such as the same-subject *ex-vivo* MRI or the population-typical reference atlas (Woodward et al., 2017), we aimed to reconstruct the true shape of the subject brain and to avoid the classical curvature recoverability problem of sectioned objects. This atlas-informed reconstruction (Lee et al., 2018) improved reconstruction accuracy compared to the atlas-uninformed neighbor-to-

25

511   neighbor method, as well as reduced the deformable metric cost. The impact of the *ex-*

512   *vivo* MRI constraint on the 3D reconstruction is shown in Figure 6 (right). A visible

513   distortion is present in the MRI-unguided reconstruction. The degree of shrinkage is 7%

514   from *in-* to *ex-vivo* MRI and 1% from *ex-vivo* MRI to histology. This distortion is

515   corrected by a MRI-guided method using a reference atlas. The MRI-constrained

516   alignment of the Nissl sections produces a Nissl volume which closely resembles the

517   convex hull of the same-subject MRI, leading to accurate parcellation of the brains in

518   question.

519

520

521

522   **Results**

523

524   Brain volumes generated by the combined pipeline were further subjected to automated

525   cross-modal registration and atlas segmentation, to obtain a regional connectivity matrix.

526

527   **Connectivity mapping**: The registration process permitted brain surface reconstruction

528   (Video 1), 3D visualizations of projections, and virtual cuts in other planes of section

529   than the original Coronal sections (Figure 6 (right)). After segmentation and registration,

530   we derived quantitative values of tracer signals within each region. We developed an

531   image processing method for detecting axonal and dendritic fragments in images, and

532   applied it to each high resolution section (0.46μm) to segment the anterograde projections.

533   The segmented pixels were appropriately weighted to create an isotropic 3D summary of

534   the projections (Markov et al., 2014). We developed an automatic cell detection method

535   (Pahariya et al., 2018) to segment somata labeled by the retrograde label Fast Blue

536   throughout the entire brain. Injection sites were separated out from the rest of the brain.

537   The projection strength between each target and source region was quantified as the

538   fractional number of voxels containing tracer label.

539

540   The registration process together with process and cell detection methods allowed us to

541   obtain intermediate resolution, annotated images for each tracer and to review the atlas

542   parcellation. Figure 7 shows the result of three fluorescent tracer injections in the same

543   animal and their origin/projections, resulting in one column and two rows in the putative

544   connectivity matrix. In this example, Fast Blue, AAV-GFP and AAV-TdTOM were

545   injected in V6, V1, and V6 visual cortex respectively. Automatic process detection

546   identified projection targets from V1 to various regions, including the most prominent

547   projections detected in V5 and dorsal lateral geniculate nucleus (DLG). Projection targets

548   from V6 included the lateral pulvinar (LPul) and medial pulvinar (MPul) among other

549   targets. Automatic cell detection for the Fast Blue tracer identified the regions projecting

550   to V6 including prominent projections from A6DC, A31, and inferior pulvinar (IPul).

551
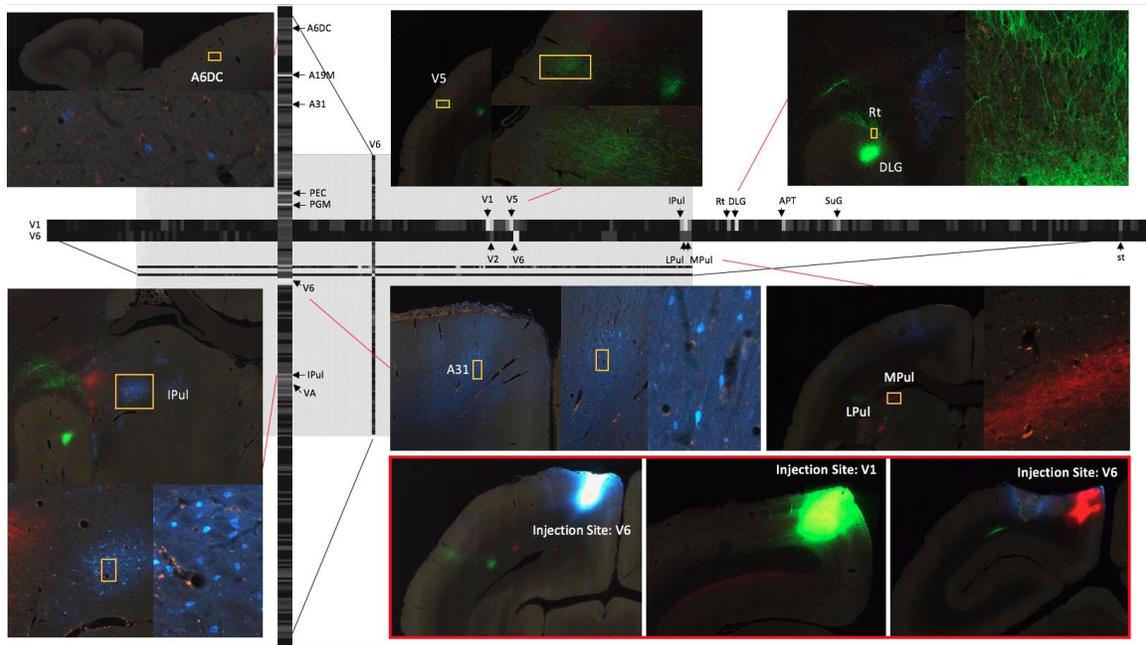
Figure 7. A part of the connectivity matrix identified with tracer injections in one sample brain. The retrograde tracer Fast Blue was injected in V6 and found in high density in several regions such as lPul and A31. AAV-GFP was injected in V1 and AAV-TdTOM in V6 and show clear projections to the thalamus and other visual areas. Each row contains all projections to different brain regions originating from those AAV tracers. The magnified images highlight some clear origin/projections from the injected tracers in the connectivity matrix.

Discussion

We have described a high throughput, standardized pipeline integrating experimental and computational elements into a unified system and workflow for processing tracer-injected Marmoset brains, representing an essential step towards producing a whole-brain mesoscale connectivity map in an NHP. The pipeline combines the well-established neuroanatomical protocols with automated instrumentation and a software system for greatly improving the efficiency of the techniques compared to conventional manually-

569 intensive processing. Access to high-quality *in-vivo* and the *ex-vivo* MRI provided us

570 with important auxiliary data sets facilitating re-assembly of the section images and atlas

571 mapping, thus ameliorating the challenges arising from increased individual variations in

572 brain geometry in an NHP compared with laboratory mice.

573

574 It is important to compare with other microscopic methods that have become established

575 in recent years for light-microscope based anatomy, including serial block-face two

576 photon scanning microscopy (Denk & Horstmann, 2004; Osten & Margrie, 2013;

577 Svoboda & Yasuda, 2006) and light sheet microscopy (Glaser et al., 2018; Nikon, 2018),

578 as well as knife-edge scanning microscopy (Mayerich, Abbott, & McCormick, 2008).

579 While these methods have important advantages, particularly the reduced need for

580 section-to-section registration to produce the initial 3D volumes for further analysis, the

581 classical methods have the important advantage of carrying through conventional

582 histochemistry without major protocol alterations, producing long-lasting stains and

583 precipitates that can be imaged using brightfield microscopy. Classical Nissl and myelin

584 stains remain the gold standard for cytoarchitectonic texture-based determination of

585 precise brain region location and delineation. These series are produced routinely with

586 ease in the pipeline. The thin physical sections can be imaged rapidly in whole-slide

587 imaging scanners and at relatively high numerical aperture (resolution in light sheet

588 microscopy is comparatively limited due to reduced NA in the bulk of the sample).

589

590 **4.1 Individual Variation in Brain Anatomy in the Marmoset:**

591

592 Previous studies aimed at generating population based atlases non-human primates

593 (Black, Koller, Snyder, & Perlmutter, 2001; Black, Snyder, Koller, Gado, & Perlmutter,

594 2001; Feng et al., 2017; Hikishima et al., 2011; Quallo et al., 2010) have focused on

595 mapping individual brains to a common mean template. Individual variations were

596 addressed in terms of variation in stereotaxic coordinates of major landmarks such as

597 sulci (Black, Koller, et al., 2001; Black, Snyder, et al., 2001; Hikishima et al., 2011). A

598 few studies have explicitly reported variations in brain sizes (Hikishima et al., 2011) but

599 we did not find an analysis of variations of individual regions, or co-variations across

600 regions.

601

602 The data gathered in the project permits an a-posterior analysis of individual variations in

603 brain anatomy and cytoarchitecture. While a comprehensive analysis has to be left to a

604 future study using this data, we summarize a few observations based on a partial analysis.

605 Within a sample of 26 cases, the whole brain volume had a median of 8222.5 mm^3 with a

606 median absolute deviation (MAD) of 319.4 mm^3. In comparison to the Paxinos/Hasikawa

607 (Brain/MINDS) template (Hashikawa et al., 2015; Hikishima et al., 2011; Woodward et

608 al., 2017), our animals were older and mostly heavier than the template brain animal. Yet

609 the brain sizes were similar to the template brain. We did not find a significant

610 relationship between whole brain volume and age or body weight (see Appendix 10)

611 within our data set. Nevertheless, some individual compartment sizes significantly

612 departed from the template brain (e.g. the Hippocampal formation showed a consistently

613 smaller size), indicating that the template brain may not be representative of a population

614 average. Quantitative analysis of the covariation of cytoarchitectonic structure across the

615 whole marmoset brain, in a significantly sized sample, is possible with the data gathered

616   in the current study and will be carried out in the near future. We expect that the

617   reference atlas may need to be revised based on the results of such a study.

618

619   **4.2 Injection Size variations and localization within compartments:**

620

621   Based on a preliminary analysis, 73% of the injections placed are localized within atlas-

622   determined anatomical compartments, whereas 27% showed some spread across

623   boundaries. Manual analysis of a subset of 15 injections showed diameters in the range

624   0.8mm-2.5mm, indicating rough correspondence with the desired grid spacing. Among

625   these 15 injections, 6 had tracer spread beyond the compartment boundary. On average,

626   for these 6 injections, about 68% of the volume was restrained within the same region as

627   the injection center, while about 32% of the volume leaked outside to adjacent regions.

628

629   **4.3 Combining injections with those from previous studies to increase sample size:**

630

631   We were able to combine subsets of the injections placed in this study with injections in

632   previous studies, as well as data gathered in collaborating laboratories, to generate and

633   test specific hypotheses, indicating the utility of the data gathered in the project (Lee et

634   al., 2018; Majka et al., 2018). In addition, analysis of injection centers show

635   proximity/overlap of injections from a previous data set from the Rosa laboratory for

636   which 3D spatial information is available (Appendix 10). This should permit virtually

637   increasing N for this project.

638

4.4 Completion of Brain-wide Coverage in the Marmoset:

An estimate of the total number of injections that will provide brain-wide coverage, in the hybrid grid-approach adopted in the paper depends on the lower cutoff placed on atlas compartments to be injected. To obtain an upper bound, we assume a cutoff of 0.8mm^3 (corresponding to the smallest injections we placed so far), which corresponds to 356 sites (712 injections). So far, 190 injections have been placed in 49 brains. To cover the rest of the brain, 264 more injections would be placed in the cortex, and 258 injections in subcortical regions and cerebellum. This would require 131 brains. The current pipeline has achieved a maximum capacity of 2 brains/month. At this rate, a complete marmoset mesoscale connectivity map would be available by 2024. However, we expect that the process can be speeded up considerably by multiple groups working together in a collaborative manner using similar methods. Such a project would necessarily need to have international scope and can be expected to be transformative for our understanding of primate brain architecture.

4.5 Larger Brains:

The pipeline described here is for 1x3 inch glass slides that fortunately are large enough to accommodate Marmoset monkey brains in coronal section. The pipeline can be generalized in the future to 2x3 inch slides, which can handle larger brains (such as that of Macaque monkeys), with a few technical innovations, importantly stainers/coverslippers for the larger format slides. This should allow the easy and economical neurohistological processing of larger sized vertebrate brains, opening up the

662 possibilities of applying modern computational neuroanatomical techniques to a

663 significantly broader taxonomic range of species, allowing for the study of comparative

664 neuroanatomical questions with unprecedented computational depth.

665

Acknowledgements

666

667

690

691   Competing interests: The authors declare no competing financial interests

692

693 **Appendix 1**

694

695 **MRI Method**

696 During MRI, the animal was anaesthetized using 3% (+/- 1%) isoflurane in oxygen and

697 received an intraperitoneal injection of sterile saline (3ml) to avoid dehydration during

698 the procedure. Throughout the entire procedure, a mixture of oxygen and 2% (+/- 0.5%)

699 isoflurane was administered to maintain anesthesia. A custom-made head holder (Qualita

700 Ltd., Saitama, Japan) was used to fix the marmoset head within the imaging tube, such

701 that the rostral-caudal axis of the head was stereotaxically aligned with the tube. A small

702 glass capillary with a contrast agent was used in each ear bar, such that the positions of

703 the ear bars would be visible in the MRI images. A heating pad was used to maintain the

704 body temperature. Heart rate, blood oxygen saturation levels, rectal temperature and

705 respiration rate were continuously monitored and recorded every 10 minutes.

706

707 During *in-vivo* **MR** imaging, high-resolution 3D T1 mapping was carried out using a

708 Magnetization-Prepared Rapid Gradient-Echo (MPRAGE) sequence (Liu, Bock, & Silva,

709 2011) with a repetition time (TR) = 6000 ms, inversion times (TI) = 150, 1300, 4000 ms,

710 (TE (echo time) = 2 ms TD (time-domain) = 9 ms) and a nominal flip angle (FA) = 12

711 degrees. Imaging planes were axial slices with FOV = 48.0×38.4×22.6 mm at matrix size

712 = 178×142×42. T2-weighted images (T2WI) were acquired using a rapid acquisition with

713 relaxation enhancement sequence (J. Hennig, A. Nauerth, & H. Friedburg, 1986) with the

714 following parameters: repetition time/echo time echo = 4000 ms/22.0 ms, RARE factor =

715 4, averages = 3, field of view = 48 mm × 48 mm, matrix = 178 × 178, slice thickness =

716 0.54 mm.

717

718 Diffusion weighted images were acquired by a pulse-field gradient spin-echo (PGSE, the

719 Stejskal-Tanner diffusion preparation (Stejskal & Tanner, 1965)) based on echo planner

720 imaging sequences along 30 MPG axes and were acquired with the following parameters:

721 b-values = 1000 s/mm^2, TR = 4000 ms, TE = 25.57 ms, averages = 3, k-space segments =

722 6, matrix = 128 x 128, FOV = 44.8 x 44.8 mm^2, and slice thickness = 0.7 mm. The DTI

723 map was acquired using a method adapted from Fujiyoshi et al. (Fujiyoshi et al., 2016).

724 An eigenvector associated with the largest eigenvalue λ1 was assumed to represent the

725 local fiber direction. Three DTI maps were reconstructed from the data as follows: axial

726 diffusivity (AD) = λ_1, radial diffusivity (RD) = ($\lambda_2 + \lambda_3$)/2, and mean diffusivity (MD) =

727 ($\lambda_1 + \lambda_2 + \lambda_3$)/3.

728

729 For the *ex-vivo* **MR** imaging following perfusion, the brain was immersed in an

730 electronic liquid (Fluorinert FC-72; 3M) in a 32 mm ID acrylic tube. High resolution T2-

731 weighted images (T2WI) were acquired using a rapid acquisition with relaxation

732 enhancement sequence (Jürgen Hennig, A. Nauerth, & H. Friedburg, 1986) with the

733 following parameters: repetition time/echo time echo = 10000 ms/29.36 ms, RARE factor

734 = 4, averages = 16, field of view = 36 mm × 30 mm, matrix = 360 × 300, slice thickness

735 = 0.2 mm. Diffusion weighted images were acquired by a pulse-field gradient spin-echo

736 (PGSE, the Stejskal-Tanner diffusion preparation (Stejskal & Tanner, 1965)) based echo

737 planner imaging (Mansfield & Pykett, 1978) sequence along 128 MPG axes which was

738 acquired with the following parameters: b-values = 1000, 3000 and 5000 s/mm^2, TR =

739 4000 ms, TE = 28.4 ms, averages = 2, k-space segments = 10, matrix = 190 x 190, FOV

740 $= 38.0 \times 38.0 \text{ mm}^2$, and slice thickness $= 0.2$ mm.

Appendix 2
741

742

743 **Tracer Injections**

744 Our project plans to cover 255 injection sites in the marmoset brain, one anterograde and

745 one retrograde tracer at each site, evenly distributed across the grey matter of the right

746 hemisphere of the marmoset brain. The stereotaxic coordinates of all injection sites were

747 systematically chosen using an MRI-based atlas (Hashikawa et al., 2015) and the

748 injection location choice was based on an established algorithm (Mitra, 2014). Briefly,

749 the right hemisphere was separated into 255 equal sized parcels, respecting anatomical

750 boundaries. The plan resulted in 199 injection sites within the cerebral cortex, and 56

751 injection sites in the subcortical regions. Each subcortical region was evaluated in terms

752 of the structure's volume. The injection was then placed based on the grid space modeled

753 for the individual structure of interest.

754

755 We used a borosilicate micropipette with an outer diameter of 20-30μm as a vector of

756 injection. The tracer was placed at each appropriate depth with an injection speed of

757 20μl/min. Anterograde tracers, AAVTRE3TdTom (0.3 μl) and AAVTRE3Clover (0.3 μl)

758 and retrograde tracers, Fast Blue (FB, 0.3 μl 5% solution in distilled water; Funakoshi;

759 Tokyo, Japan) and biotin conjugated Cholera toxin subunit B (CTB, 0.6 μl 1% Enzolife,

760 New York, USA) were used.

761

762   Post recovery, the animal was housed individually and monitored throughout the 4-week

763   incubation period. The animal received a non-steroidal anti-inflammatory (Oral Metacam;

764   0.05 mg/kg, Boeringer Ingelheim) for three days immediately following the surgery.

765

766   **Appendix 3**

767

768   **Perfusion/Embedding**

769   After the 4-week viral incubation period, the animal was euthanized and perfused. The

770   marmoset was injected with Diazepam (Pamlin:2mg/kg), Ketamine (10mg/kg), then

771   pentobarbital (80mg/kg) to anesthetize. The animal was then perfused using an 18" oral

772   gavage needle that entered the left ventricle and terminated at the aorta through the aortic

773   valve. 500mL of heparinised PBS was used (50ml/min) to remove the blood supply prior

774   to the beginning of asystole to ensure that no clotting occurred; afterwards 500mL of 4%

775   PFA in 0.1M PB was used (70ml/min) for fixation purposes.

776

777   After extraction, the brain was submerged in 4% PFA overnight. The brain was then

778   transferred to 0.1M PB and underwent a post-mortem *ex-viv*o MRI. Following the *ex-vivo*

779   MRI, the brain was transferred into 10% sucrose in 0.1M PB overnight and then placed in

780   30% sucrose in 0.1M PB for means of temperature protection.

781

782   A rectangular base mold was custom made with Polylactic Acid (PLA) at 3×4×5 mm. A

783   slit was opened from the bottom of the mold and an additional piece of PLA was cut to fit

784   into the slit for easy removal of the brain block after the freezing process. A 3D-printed

785   brain mold made from MR images of several marmoset brains (Hashikawa et al., 2015)

786   was attached to a positioning bar with its rostral side facing the arrow direction (Figure 1).

787   A custom freezing platform, also 3D-printed, secured the base mold flat and allowed the

788   positioning bar for the brain mold (dorsal side down) to adjust vertically.

789
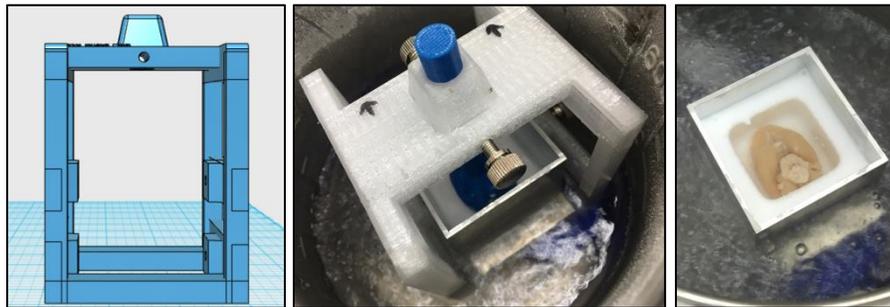
790

791   Appendix figure 1. **Rectangular base mold was designed and printed to serve as a freezing platform.** The freezing
792   platform was used to control the position of the brain mold to the base mold during freezing. The positioning bar is
793   adjustable to allow ease of insertion and removal of the brain mold from the base mold.

794

795   While the brain and base molds were attached to the freezing platform, the positioning

796   bar was adjusted to lower the brain mold dorsal (down) side to 2 mm from the slit.

797   Embedding medium Neg50 (Richard Allen Scientific, Waltham, MA) was then added

798   into the base mold until it slightly touched the dorsal (down) side of the brain mold. The

799   freezing platform, with the base and brain mold still attached, was placed in a -80 $^{\circ}$C

800   freezer until the Neg50 was solid.

801

802   When the Neg50 was fully frozen, the brain mold was briefly thawed by a heat gun to

803   remove it from the base mold. The surface temperature of the brain mold cavity was kept

804   at -2 $^{\circ}$C to hold the brain shape while leaving the Neg50 solid. Additional Neg50 was

805 then added to the base mold, filled to a volume to sufficiently immerse the brain, and left

806 to thermally stabilize for 15 seconds. The brain was removed from the 30% sucrose in

807 0.1M PB solution and dried for 30-45 seconds before being carefully placed within the

808 Neg50 filled base mold with the ventral side of the brain facing up at a 0° horizontal

809 plane. The base mold was then placed in dry-ice chilled 2-methylbutane until all the

810 Neg50 was uniformly frozen. Finally, the base mold was thawed by a heat gun to remove

811 the brain block from the base mold apparatus, placed in a properly labeled freezer bag,

812 and stored in a -80 ^{o}C freezer.

813

814 **Appendix 4**

815

816 **Cryo-sectioning**

817 The cryostat's stage was modified to accommodate the larger dimensions of a cryo-

818 embedded brain block and aided in stabilizing the cryostat's chuck and blade (Figure 2a

819 and 3b). The UV-LED device was arranged in 4 rows of 11 LEDs in a parallel resistor

820 network to provide uniform UV intensity across the surface of the slides. Each array was

821 connected to a single 6V DC power source and regulated by an on-off timer controller

822 using a Raspberry Pi 3 (Raspberry Pi, 2016). Figure 2c shows the setup of the UV station

823 within the cryostat.

824
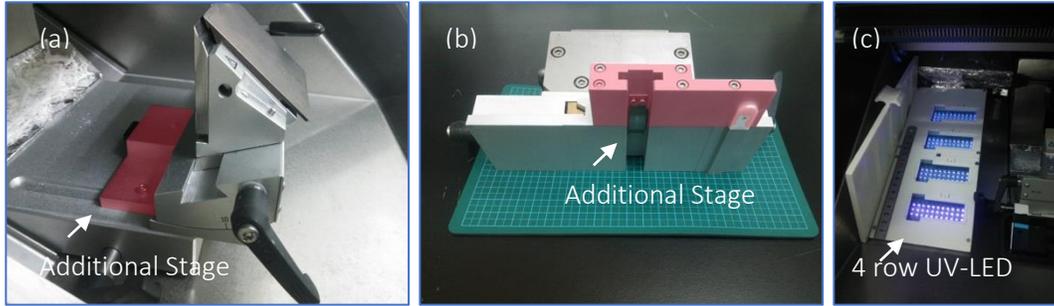
Appendix figure 2. **Modified cryostat chamber to accommodate for larger brain block.** (a,b) Additional stage shown in pink was attached to the original cryostat stage to increase the room space and to aid in stabilization of the cryostats chuck and blade. (c) a 4 row UV-LED device to provide UV intensity across the surface of the slides by an on-off timer controller using a Raspberry Pi.

Appendix 5

Histology (Staining)

The slides for **Nissl** staining were processed through an automated Nissl staining protocol beginning with a thionin solution: 1.88g thionin chloride (TCI, T0214) in 750mL De-ionized H_2O (DiH_2O), 9mL of glacial acetic acid (WAKO, 012-00245), and 1.08g sodium hydroxide pellets (Sigma-Aldrich, 221465-500G). The slides then underwent three washes of DiH_2O followed by dehydration in increasing concentrations of ethanol 50%, 70%, 95% 100% and finally Xylene, (Nissl, 1894; Pilati, Barker, Panteleimonitis, Donga, & Hamann, 2008) followed by automatic cover-slipping.

The **myelin** staining technique used a modified ammoniacal silver impregnation technique originally developed by Gallyas (Gallyas, 1979). Instead of the standard protocol of implementing the technique on free floating sections, the protocol was

845   applied to the slide mounted sections. After the physical development of the myelin stain,

846   the tissue was manually inspected for staining and morphological quality. The slides were

847   then put on a drying rack for 24 hours and were dehydrated with ethanol followed by

848   automatic cover-slipping.

849

850   The **CTB** designated slides were manually loaded into Immunohistochemistry (IHC)

851   basins (Light Labs, LM920-1). The basins were filled to ½ of their volume with tap water

852   to maintain humidity levels. In our CTB-DAB (3,3'diaminobenzidine) protocol , the

853   solutions were pipetted with ~800uL onto each slide. The first step, blocking, consisted

854   of 15 mL methanol (Nacalai Tesque, 21915-35), 480mL 1xPBS, and 1.25mL hydrogen

855   peroxide H_2O_2 (Wako, 081-04215) was shaken and sprayed onto the slides. The protein

856   block was made of 1% v/v triton X-100 (Sigma Aldrich, X100-500G), 3.5% v/v normal

857   rabbit serum (Vector Labs, S-5000) in 1xPBS for 30 minutes at room temperature (RT),

858   followed by 1xPBS rinse 3 times and pressure assisted drying. The primary antibody step

859   consisted of 2% v/v goat anti-CTB (List Laboratories, #703) (1:2500 concentration),

860   0.3% v/v triton X-100, 3% v/v normal rabbit serum in 1xPBS which was left overnight at

861   RT with the IHC basins covered to preserve liquid levels and ambient humidity within

862   the basin. Once the slides went through a 1xPBS rinse 3 times and pressure assisted

863   drying, the secondary antibody made up of 0.4% v/v biotinylated rabbit-anti-goat IgG

864   (H+L) (Vector Labs, BA-5000) (1:250 concentration), 1% v/v normal rabbit serum, 0.3%

865   v/v triton X-100 in 1xPBS was added and left for two hours at RT. After another 1xPBS

866   rinse 3 times and dry cycle the Avidin-biotin complex elite kit (ABC, Vector Labs, VEC-

867   PK-6100) was placed on the slides and left to incubate for three hours at RT. The ABC

868 kit was used with equal volumes of avidin and biotin, 1% v/v avidin and biotin were

869 made 30 minutes before use.

870

871 Our DAB-Nickel Cobalt (DAB-NiCo) staining protocol used 1% w/v DAB (Apollo

872 Scientific Limited, BID2042) 1% w/v ammonium nickel (II) sulfate hexahydrate (Santa

873 Cruz Biotechnology, sc-239235), 1% w/v Cobalt (II) Chloride hexahydrate (Sigma

874 Aldrich, 255599-500G), and 0.00003% v/v H_2O_2. The DAB, Ni, Co and H_2O_2 were

875 prepared with a DiH$_2$O in 50mL conical tubes and filled to 50mL. 150µl of hydrochloric

876 acid (Nacalai Tesque, 18320-15) was added to the 50mL conical DAB tube to ensure

877 homogeneity. 800mL of 1xPBS was prepared then added to a 2L Erlenmeyer flask placed

878 on a stir plate, the 1% DAB-NiCo solutions were added to the Erlenmeyer flask, and was

879 homogenized with a stir rod. 350µL of 10M NaOH (AppliChem, A3910,1000) was added

880 to bring the final pH of the DAB-NiCo to 7.1-7.4pH.

881

882 A glass basin large enough to contain 1L of liquid was used inside a fume hood and all

883 slides within the IHC basins were manually loaded into slide racks and placed within the

884 basin. The H_2O_2 was added to the flask just before staining to catalyze the DAB-NiCo

885 reaction. The final working solution was poured from the flask into the basin where the

886 slides had been placed. The incubation time (~10min) was monitored manually until the

887 injection site could be visualized as the affected cells turned black. Manual monitoring

888 was used to make sure that the signal-to-background noise ratio was kept from being

889 deleterious to the final stain quality. The slides were then transferred through 3 full

890 emersion washes of 1xPBS.

891

892   The slides were left on a drying rack overnight at RT and were put through a Giemsa

893   counterstain after a 24-hour period. The Giemsa counterstain consisted of a 3:7 ratio of

894   30% Giemsa (Nacalai Tesque, 37114-35) and 70% DiH_2O, a 1xPBS wash, 1% w/v

895   ammonium molybdate (Sigma-Aldrich, A1343-100G) wash, a second 1xPBS wash

896   followed with ETOH dehydration. The slides were then cover-slipped and put into drying

897   racks for 24 hours.

898

899   # Appendix 6

900

901   **Computational Infrastructure**

902   All of data machines within the laboratory were connected to data center using a 10g

903   network for further analysis by a 16 node high-performance computing (HPC) cluster.

904   Storage nodes were configured as Raid6 devices and provided 78TB of useable disk

905   space each for a total of 156TB. The theoretical maximum transfer rate of the 10g

906   network is 900 MB/s; however, the rate limiting process was due to the hard disk writing

907   speed of each machine. The current average transfer speed is about 250-520MB/s.

908

909   The data processing (cropping and converting) in the data-acquisition server began when

910   the Nanozoomer slide scanning was completed. The processed data were transferred to a

911   central repository for quality control. This configuration could improve the overall

912   process rate from 50% of the theoretical maximum up to 80% in performance. As shown

913   in Figure 3, an entire network and computation pipeline setup was adopted in the RIKEN

914   Marmoset Neural Circuit Architecture Laboratory.

915

916
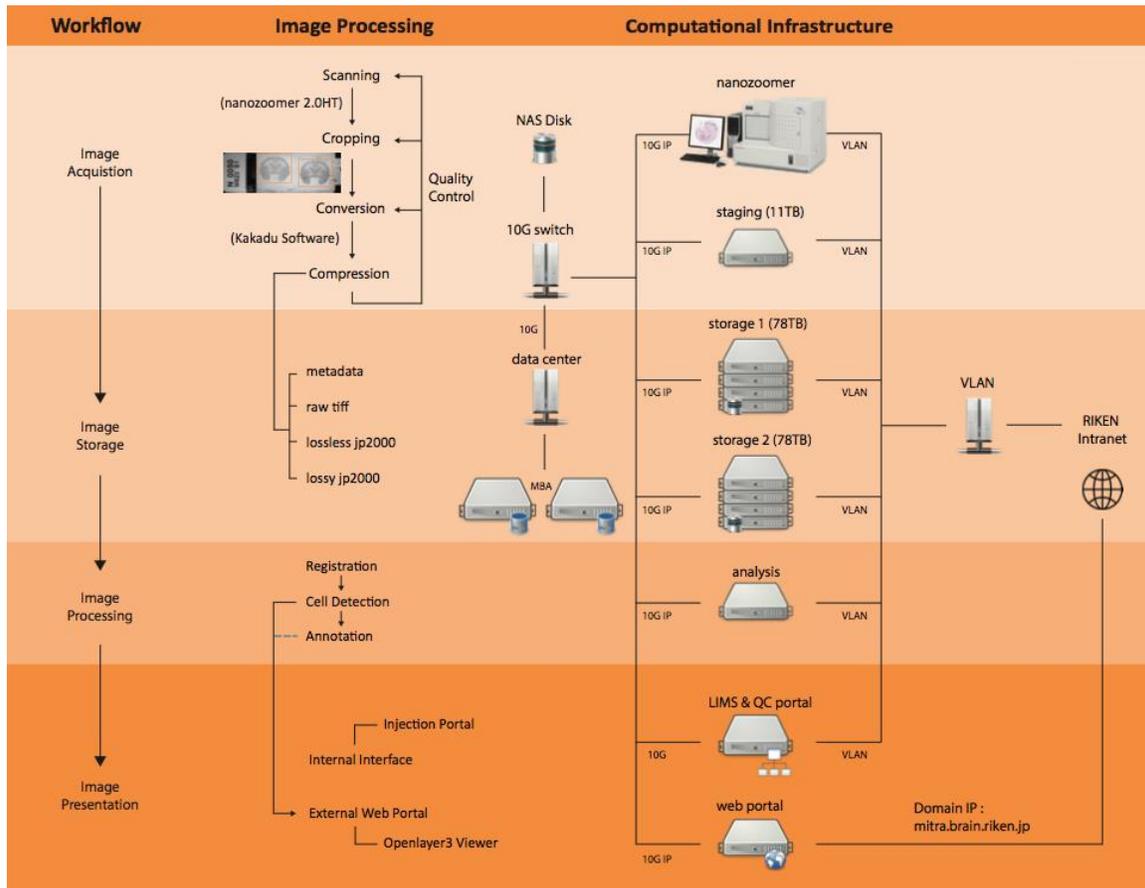
917

918   Appendix figure 3. **Computational pipeline with the network structure to perform a high-throughput data flow and**

919   **process.** There were four steps of workflow involved in this pipeline including image acquisition, storage, processing and

920   presentation. With these steps, generating a whole marmoset brain dataset with high production rate and superior system

921   performance for large data communication was possible. Each server node was connected to one 10g network for data

922   communication and one external network for remote access.

923

924

925 # Appendix 7

926

927 **Computational Processing**

928 The computational pipeline builds upon the pipeline originally developed by the CSHL

929 Mitra Lab for the mouse and was modified to meet the marmoset tissue size and structure

930 (Figure 4). For each tissue section, the system produced (1) a meta-data file with all the

931 relevant information (cropping and conversion processing); (2) a cropped ROI as a TIF

932 format for image inspection; (3) a down sampled JPEG2000 image for rapid access for

933 the data on the web portal; (4) an uncompressed raw data file. Our automatic detection

934 algorithm for the cropping box placement in images performs at a 100% success rate in

935 both brightfield and fluorescence sections. The image format used custom scripts based

936 on the Kakadu toolkit (Kakadu, 2016). For any given complete marmoset brain, there

937 were a total of ~1700 sections mounted on ~900 slides.

938
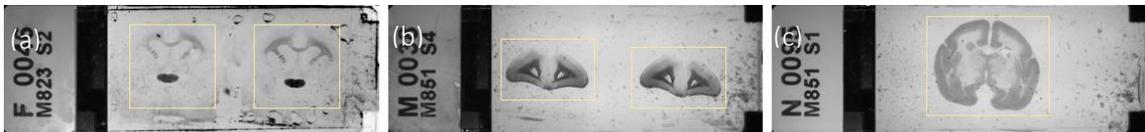
939

940 Appendix figure 4. **Example of a Nanozoomer macro image determining the cropping ROIs.** (a) fluorescence slide (b
941 and c) brightfield slides shown with yellow cropping box.

942

943 This project developed and utilised an online quality control (QC) service. The QC

944 service was employed to assess the quality of each image and determine if the re-imaging

945 of a slide or the re-injection of an entire brain was needed. Correcting or improving the

946 pipeline process was an evolutionary and organic process and flagging unwanted sections

947 or materials to reduce unnecessary post-processing was a key step. The researcher had the

948   option to view all the sections of the series (with the comparison of a micro image) and to

949   edit the fields for QC such as tissue damage, missing sections and poor cover-slipping

950   alignment. Once flagged, the QC service would automatically remove the sections from

951   the dataset allowing for proper processing of the image analysis such as 2D alignment

952   and 3D reconstruction.

953

954   The images of brain slices from histological processing were fed directly into the

955   computational process. The post processing data involved several steps from image

956   cropping and image conversion to 2D alignment and 3D reconstruction. This was a major

957   departure for image analysis. Acquired image datasets were written into a propriety

958   image format, JPEG2000. In the case of a JPEG2000 image, the decompression was $\approx$

959   75-90 MB for fluorescence images and brightfield images (Nissl, myelin and CTB). After

960   the proper data acquisition, automatic image processing/analysis was performed. The

961   sections across all brains were registered into a common space. This registration was

962   based on Nissl-stained sections for structural information and *ex-vivo* MRI as landmarks

963   such that all sections were able to align to each other and produce a shape similar to that

964   of the same subject reference (*ex-vivo* MRI) while maintaining coherence and continuity

965   from section to section. A variant of the large deformation diffeomorphic metric mapping

966   (LDDMM) algorithm was employed to compute nonlinear mapping between

967   Brain/MINDS Nissl atlas and the reconstructed target Nissl, followed by recently

968   developed registration methods (Lee et al., 2018).

969

Appendix 8

Processing Rate

Based on the individual marmoset brain anterior-posterior length measured by ex-vivo MRI, the number of sections (20µm/section) was determined and the processing time at each step was recorded. At each step of histological processing, a small portion of brain sections were excluded from the subsequent processing based on manual quality control inspection. The final processing success rate for each series was measured by the percentage of obtained sections, shown in Figure 5.

Section retained in 4 series
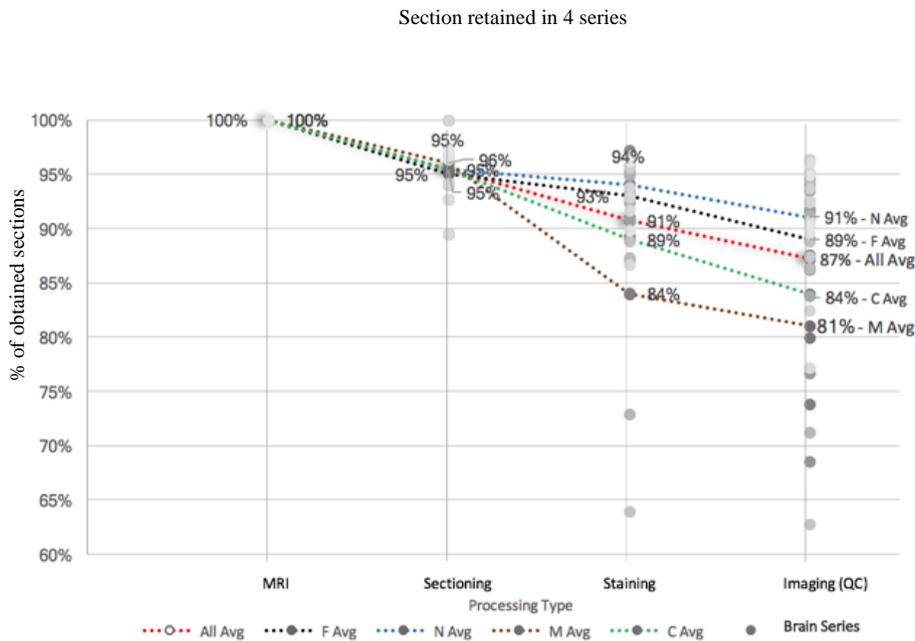
Appendix figure 5. **A pipeline processing rate with four series staining (fluorescence, Nissl, myelin, CTB) based on the latest 10 datasets.** Each series starts with 100% full rate (based on the calculation from ex-vivo MRI and the number of sections needed as well as calculated by measuring at 20um each) and reduces by a percentage based on unavoidable reasons such as poor staining or section peeling. The figure shows that there is high processing rate starting with Nissl (91%), fluorescence (89%), CTB (84%), to myelin (81%). The average processing rate is 87% in total.

Appendix 9

988

Grid-based Approach and Plan for Whole-brain Mesoscale Circuit Mapping

990

    A. Adaptive Grid-based injection plan: distribution of injection targets over the grey matter.

993

In order to obtain a data set addressing the question of whole-brain mesoscale connectivity, we adopted the approach of injecting on a systematic grid-based plan throughout the whole brain's grey matter. The grid-based approach was originally established for the Mouse Brain Architecture project, with an initial regular grid with 1mm injection spacing, adapted to avoid region boundaries (Grange & Mitra, 2011). The Marmoset brain is larger than the Mouse brain and a similarly dense set of injections would be prohibitive to carry out in terms of numbers of animals required. We therefore expanded the grid spacing to 2mm. Note that our plan is not strictly a regular grid as such a grid would also generally overlap with region boundaries. We started with an initial regular grid, then shifted/adapted grid points to avoid boundaries.

1004

The process is not entirely automated, as the atlas compartments are heterogeneous, and we adapted injection placement by actual visualization of the compartment volumes. In addition, there is also individual variability between brains, and injections themselves have size variations (e.g. due to differential fluid transport properties in different brain regions). We addressed the question of individual variation in part using *in-vivo* MRI

1010   guidance of injections, particularly for sub-cortical nuclei. We also tried to ensure that the

1011   injection surgeries were performed by expert neuroanatomists with knowledge of

1012   stereotactic injections in the specifically targeted regions of the Marmoset brain. In this

1013   way we attempted to perform better than a regular geometrical grid and accounted

1014   partially for animal-to-animal variations.

1015

1016   For grid planning we adapted the Paxinos/Hashikawa atlas as a starting template

1017   (Hashikawa et al., 2015; Hikishima et al., 2011; Woodward et al., 2017), and initially

1018   placed a 3D 2-mm grid covering all the grey matter areas, which yielded 271 injection

1019   centers in one hemisphere. This analysis missed some of the smaller structures which

1020   have volumes less than 8mm^3. However, some structures in the reference atlas are very

1021   small and not practical to inject. To determine a size threshold for future planning

1022   purposes we examined the actual sizes of the injections placed. Accounting for size

1023   variations in the tracer injections, we have found that a diameter of injection spread

1024   diameter as small as 0.8 mm and as large as 2.5 mm (assuming spherical spread; see

1025   analysis below) could be achieved in practice. We therefore could plan at least 1 injection

1026   center for each brain region with volume ranging from 0.27 mm^3 to around the grid size

1027   of 8 mm^3. Figure 6 presents the total number of injections, and the number of animals

1028   need to be involved in the experiments, with regard to different sizes of injection spread.
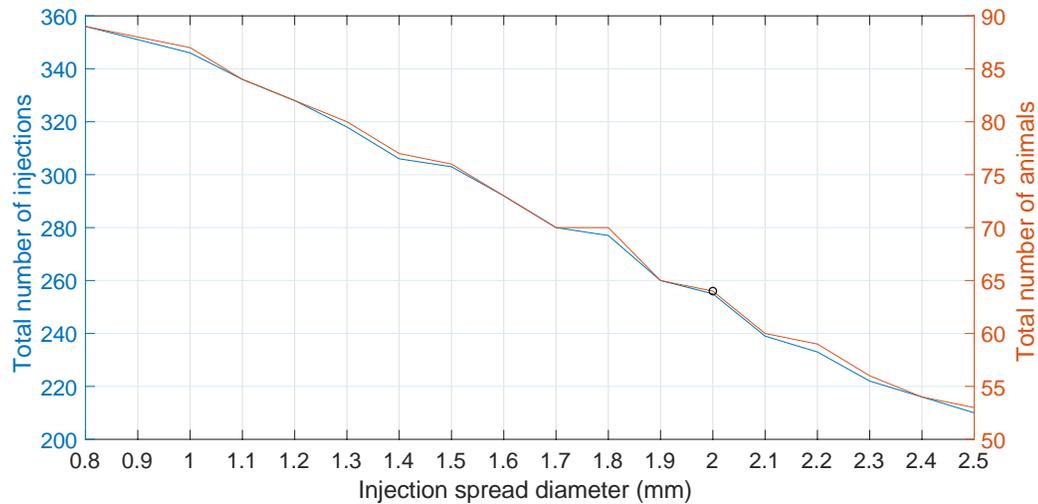
1029

1030 Appendix figure 6. **Plots presenting the total number of injections, the number of animals needed and injection**

1031 **spread diameter (mm).** Each plot represents the different sizes of injection spread in diameter (mm); the right side y-axis

1032 represents the total number of animals required to be involved in the experiments; the left side y-axis represents the total

1033 number of injections. The black circle is the cutoff where a 2-mm diameter injection spread requires 255 tracer injections

1034 throughout a total of 64 marmoset brains. The cutoff represents a reasonable balance between minimal animal use versus

1035 maximum number of tracers that can be used in this experiment.

1036

1037 Assuming a spherical injection spread with 2-mm diameter, our overall "adaptive" grid

1038 plan for injections contains a total of 255 injection centers in 241 target structures in one

1039 hemisphere's grey matter (Figure 6). Since each site in the plan is separately targeted

1040 with retrograde and anterograde tracers, this implies a total placement of 510 injections.

1041 In our plan we try to maximize the number of tracers per animal, to minimize animal

1042 number, placing 2 retrograde and 2 anterograde injections. Thus, the placement of 510

1043 injections requires 64 Marmosets. It is necessary to prioritize the larger areas (and the

1044 areas that will be less failure prone when injected), and also ideally to combine data

1045 across groups.

1046

1047   Given the considerations as described above, in the cerebral cortex, 398 injection centers

1048   cover 118 target structures, comprising 74% of the total grey matter volume (Figure 6).

1049   The largest regions such as V1 and V2 contain 33 and 15 injection centers, respectively,

1050   while small regions such as anterior intraparietal area (AIP) and temporal area 1 (TE1)

1051   have only 1 injection center each.

1052

1053   **Protocol note:** *in-vivo* MRI was performed on every animal before tracer injection to

1054   obtain *a priori* information of the individual brain's anatomy. Using the approach of

1055   Large Deformation Diffeomorphic Metric Mapping (LDDMM) (Ceritoglu et al., 2010),

1056   the marmoset brain atlas is matched to the individual's brain MRI images so as to provide

1057   guidance on the injections (see Section 2.2). In addition, for specific subcortical

1058   injections we adopted an *in-vivo* MRI based stereotaxic surgery procedure to ensure

1059   accurate placement of the injections in subcortical nuclei (Mundinano, Flecknell, &

1060   Bourne, 2016).

1061

1062   It is to be noted, that despite best efforts, it is impossible to guarantee that every injection

1063   is placed within the center of a regional boundary as designated by a reference atlas.

1064   However, we do not regard this as a fundamental obstacle to obtaining a draft

1065   connectivity map of the Marmoset brain. Our approach is conservative in that it uses far

1066   fewer animals than would be required if there was an insistence of precise placement of

1067   the injections, as this more conservative approach is inherently more lossy as well as

1068   costly in terms of animals. Secondly, the regional boundaries are themselves open to

1069   discussion and debate. Ultimately these debates need to be settled by the availability of

1070   unbiased brain-wide data sets and using an existing reference atlas to precisely place

1071   injections may occasionally perpetuate previous errors. Thirdly, our data sets are

1072   comprehensive 3D brain-wide volumes with multiple histological series, permitting both

1073   computational analysis, and expert neuroanatomists to draw their own judgments.

1074

1075   We feel therefore that the grid-based approach, while imperfect, is an important stepping

1076   stone towards understanding Marmoset brain circuits in particular and primate brain

1077   circuitry in general. It is without doubt the case that the current data set constitutes a

1078   major advance in this area. For details on target structures and number of injections,

1079   please refer to Supplementary File 1.

1080

1081   B. Grid coverage in the current data set, and considerations of tracer spread across

1082   regions

1083

1084   As of the publication of this paper, we have placed 178 injections in the cerebral cortex,

1085   including both anterograde and retrograde tracer injections (see Section 2.1), covering

1086   47% of the planned injection centers. 12 injections over 3 injection centers have been

1087   placed in the thalamus. 47 brains including 99 injections in the cerebral cortex have been

1088   processed through the experimental and computational pipeline. Manual annotation was

1089   performed to assess the fidelity of injection to the plan. 73% of the injections were

1090   restrained within the relevant anatomical boundary, while 27% injections had tracer

1091   leakage into adjacent regions. About 21% of the injections restrained within one region

1092   were within the large cortical regions including V1, V2 and V3. Among the injections

1093   with tracer spread into more than one region, about 18% (5 injections) were due to actual

1094   injection centers placed too close to the anatomical boundary. Within a sample dataset of

1095   15 injections in V1, V2 and V6 from 8 animals, we assessed the extent of tracer injection.

1096   For simplicity, we assumed a spherical spread of each tracer injection. The diameter of

1097   the injection extent ranged from 0.82 mm to 2.46 mm. When discounted by the variation

1098   in tracer volume, the diameter of injection extent based on 0.3 μl tracer volume ranged

1099   from 0.59 mm to 2.46 mm, with medians of 2.15 mm for AAV-GFP (n=5), 1.60 mm for

1100   AAV-tdTom (n=4), and 1.93 mm for FB (n=6). Among these 15 injections, 6 of those

1101   had tracer spread beyond the anatomical boundary. On average, for each tracer spread,

1102   about 68% of the volume was restrained within the same region as the injection center,

1103   while about 32% of the volume leaked outside to adjacent regions.

1104

1105   C. Future plan

1106

1107   The adaptive grid plan based on the Paxinos/Hashikawa atlas, with a cutoff 2-mm

1108   diameter injection spread, requires 510 tracer injections (anterograde + retrograde)

1109   throughout the marmoset brain, including 398 in the cerebral cortex. A total of 190

1110   injections have been placed to date in 49 animals, 178 in the cortex and 12 in the

1111   thalamus. To cover the rest of the brain with the cutoff as indicated above, 220 more

1112   injections would need to be placed in the cortex, and 100 injections would need to be

1113   placed in subcortical regions and cerebellum. This would require a total of 80 more

1114   marmosets. The high-throughput pipeline presented in the paper has a capacity of 2

1115   marmoset brains/month but this number may be scaled up by replicating equipment (the

1116   scanning being a rate limiting step). If the current rate were maintained the plan could be

1117   completed by 2022. However, by prioritizing the larger areas, the project could be

1118 completed more quickly and with fewer animals. The Figure 6 could be utilized to adapt

1119 injection/animal numbers based on an injection cutoff.

1120

1121 Appendix 10

1122

1123 Individual Variation and Impact on Injection-based Projection Mapping

1124

1125   A. Individual variation of marmoset brains: compartment sizes

1126

1127 Any brain connectivity mapping approach should address the question of individual

1128 variation. Notably, previous work on large scale mesoscale connectivity mapping has

1129 been carried out in the C57BL/6 male mouse strain controlled for age and weight. Such

1130 an approach is impractical for a primate given the numbers involved. While it is not

1131 possible to tightly control age and weight (and perform many repeats), we can still assess

1132 the extent of individual variations. Note that as our injections are tailored based on an *in-*

1133 *vivo* MRI in the same animal, overall size variations are controlled for to some extent.

1134

1135 We would also note that the stereotactic reference histological atlases used in previous

1136 studies are for an individual animal, and no real attempt has been made in the literature,

1137 to *explicitly* study the effects of individual variation on the reference atlas. In some

1138 instances, multiple brains are averaged to produce a smoother reference brain, but this

1139 does not explicitly address the issue of individual variation – it is as if in a multivariate

1140   distribution, the *mean vector* was given, but *not the covariance matrix*! In this case, not

1141   even basic statistical analysis is possible. This is a prevalent problem in the literature and

1142   it would be too much to resolve in the current study. Nevertheless, we possess a uniquely

1143   large 3D histological data set together with i*n-vivo* and *ex-vivo* MRI that will permit an

1144   unprecedented study of brain compartment size variations. We briefly commence that

1145   study here and will pursue in more detail in a future publication.

1146

1147   To account for the volumetric variation across different marmoset brains, we calculated

1148   the volumes of the whole brain based on in vivo MRI results. Note that our Marmosets

1149   are mostly female; we did not have a large enough male sample to systematically assess

1150   gender differences. Within a sample of 26 cases, the whole brain volume had a median of

1151   8222.5 mm^3 with a median absolute deviation (MAD) of 319.4 mm^3. In comparison to

1152   the Paxinos/Hasikawa (Brain/MINDS) template (Hashikawa et al., 2015; Hikishima et al.,

1153   2011; Woodward et al., 2017), our animals were older and mostly heavier than the

1154   template brain animal. Yet the brain sizes were similar to the template brain. We did not

1155   find a significant relationship between whole brain volume and age or body weight

1156   (Figure 7) within our data set.

1157
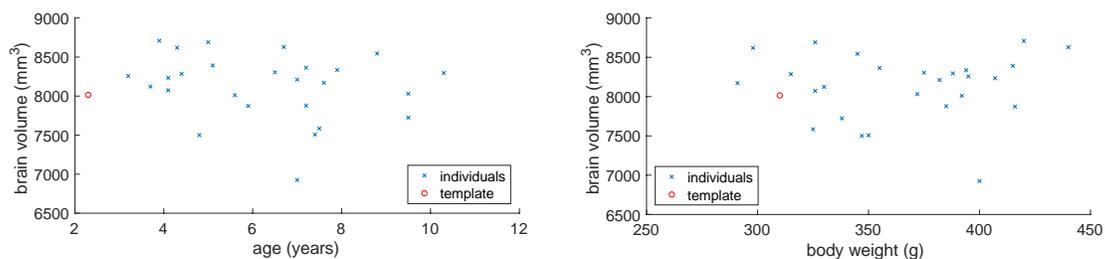
1158

1159   Appendix figure 7. **Relationship between whole brain volume and age or body weight.** The left plot shows individual

1160   marmoset variation between whole brain volume and age in comparison to the Brain/MINDS template. The right plot

1161 shows individual marmoset variation in comparison to body weight and to the Brain/MINDs template. The red circle

1162 represents the Brain/MINDs template brain and the blue crosses represents individual animals in this experiment. These

1163 plots show no significant relationship between the template brain and individual experimented brains.

1164

1165 To address the variation of specific brain compartments across animals, we estimated the

1166 volumes of individual anatomical regions based on the MRI-guided atlas mapping (see

1167 Section 2.2). By mapping the template brain regions to individual brains, we compared

1168 the results from 23 samples with the reference atlas and presented example regions

1169 including A3b (primary somatosensory cortex), A4ab (primary motor cortex), AuA1

1170 (primary auditory cortex), V1 (primary visual cortex), V2 (secondary visual cortex), HipF

1171 (hippocampal formation), Cd (caudate nucleus) and Pu (putamen). The absolute volumes

1172 of these regions (median ± MAD) are also presented. Data is provided in Appendix Table

1173 1.
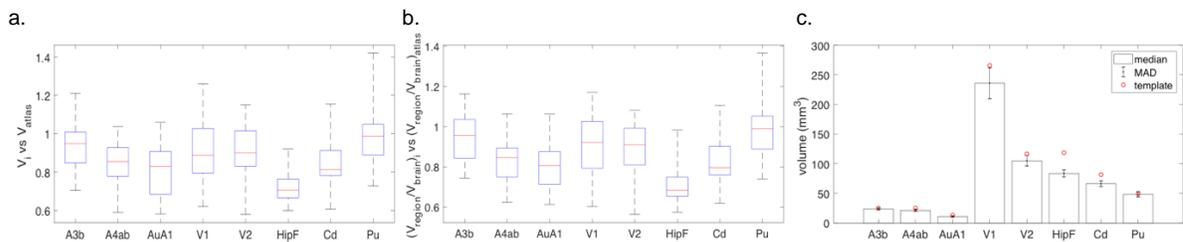
Appendix figure 8. **Comparison of individual variability of representative brain regions against the template brain.** (a)

Box plots of ratio of each brain region's volume in individual animals against its volume in the template brain, where the red

line shows the median, the lower and upper bound of the box shows the 25th and 75th percentile data, respectively, and the

whiskers extend to most extreme data points. A ratio of 1 means the same volume between the brain region in the animal(s)

involved in the current project and the template brain. A ratio lower/higher than 1 means smaller/larger brain region in the

animal in the current project compared with the template brain. (b) Box plots of each brain region's proportion in the entire

brain in individual animals against the proportion in the template brain. Similar to (a), the red line shows the median, the

upper and lower bound of box shows the 75th and 25th percentile data, and the whiskers show the most extreme data. A

ratio of 1 means the same proportion of the brain in the individual compared with the template brain. (c) Bar plot of the

absolute volume of individual brain regions across different animals. Height of the bar shows the median and the error bars

show the MAD.

		Whole brain	'A3b'	'A4ab'	'Aua1'	'V1'	'V2'	'Hipf'	'Cd'	'Pu'
V_i	median	8234	23.76	21.40	10.91	235.76	105.04	83.64	66.26	48.55
	MAD	351	2.38	2.46	1.41	36.70	12.71	7.42	7.75	5.93
V_i/V_{atlas}	median	1.03	0.95	0.86	0.83	0.89	0.90	0.71	0.81	0.99
	MAD	0.04	0.09	0.10	0.11	0.14	0.11	0.06	0.10	0.12
$(V/V_{brain})_i/(V/V_{brain})_{atlas}$	median	1	0.96	0.85	0.81	0.92	0.91	0.68	0.80	0.99
	MAD	0	0.10	0.09	0.10	0.12	0.10	0.07	0.09	0.11

Appendix table 1. **Median and MAD of each metrics evaluating the brain region volume's variability across animals.**
The table shows some of the large components in the marmoset brain.

In the context of generating population-based atlas, previous studies in humans (Yeh et al., 2018) (and non-human primates (Black, Koller, et al., 2001; Black, Snyder, et al., 2001; Feng et al., 2017; Hikishima et al., 2011; Quallo et al., 2010) mostly focused on mapping individual brains to a common template. Individual variations were addressed in terms of variation in stereotaxic coordinates of major landmarks such as sulci and caudate (Black, Koller, et al., 2001; Black, Snyder, et al., 2001; Hikishima et al., 2011). Few studies explicitly reported the variations in brain sizes involved in their studies (Hikishima et al., 2011). No study thus far has completed a region-based variation comparison as in this paper, and no study has looked at the multivariate covariance between structures. We will address these questions in a future publication.

1191   From the considerations above, it is clear that there is both significant variation in the

1192   absolute compartment volumes, and in the relative volumes normalized by the whole

1193   brain, of individual marmosets compared to the reference atlas. Thus, individual variation

1194   is present and cannot be ignored. Nevertheless, we feel that the traditional method of

1195   repeating the same injection many times in the same region, is not practical for the brain-

1196   wide connectivity mapping using the present approach. We utilize three primary tools to

1197   address questions of individual variation. First, we perform *in-vivo* MRI to ensure

1198   injection placement within the compartments of choice. Second, we use 3D histological

1199   series and diffeomorphic atlas mapping, in order to quantify the precise placement of

1200   each injection and corresponding projections, according to a mapped reference atlas.

1201   Third, as discussed below, it is possible to combine injections with data sets gathered by

1202   other investigators, to virtually increase the sample size. This is particularly feasible if the

1203   other data sets are also available in 3D atlas mapped form. This is discussed further in the

1204   next subsection. This approach of combining our project injections with data from other

1205   investigators has already led to collaborative publications (Huo et al., 2018; Majka et al.,

1206   2018).

1207

1208   B. Combining with other tracing studies

1209

1210   To gain an understanding of the possibilities of combining project data with data from

1211   other investigators, we compared 5 injection locations in 4 anatomical regions where the

1212   injections from the current pipeline and the ones previously gathered in the Rosa lab were

1213   in close proximity as evaluated by the stereotactic coordinates of the injection centers

1214   (distance ranging from 0.8-2mm) (see http://marmoset.brainarchitecture.org for all brains

1215   referred to here). All injection extents were restrained within the same brain regions as

1216   the injection centers. Figure 9 shows transverse projection of the injection locations. It is

1217   clear, that there are examples of injections that can be combined/compared across the

1218   projects. We will pursue such a combination/comparison study in a future publication.

1219
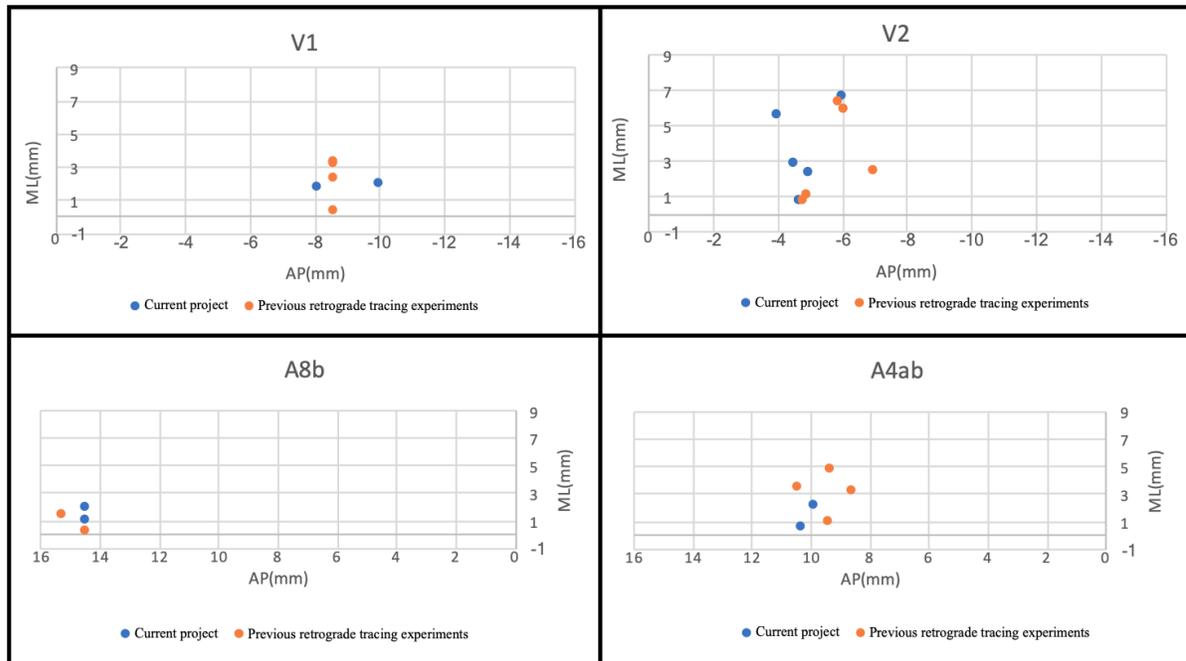
1220

1221   Appendix figure 9. **Transverse projection of the injection locations between individual brains in the current project and**

1222   **previous retrograde tracing experiments.** The similar plots (injections) presented here in V1, V2, A8b, and A4ab suggests that the

1223   current grid method is feasible and can be further analyzed across other collaborative projects.

1224

References

Allen Institute for Brain Science. (2017). Allen Brain Atlas: Data Portal. Retrieved from http://mouse.brain-map.org/

Bakker, R., Wachtler, T., & Diesmann, M. (2012). CoCoMac 2.0 and the future of tract-tracing databases. *Frontiers in Neuroinformatics, 6*, 30.

Bakola, S., Burman, K. J., & Rosa, M. G. P. (2015). The cortical motor system of the marmoset monkey (Callithrix jacchus). *Neuroscience Research, 93*(Supplement C), 72-81. doi:10.1016/j.neures.2014.11.003

Belmonte, Juan Carlos I., Callaway, Edward M., Caddick, S. J., Churchland, P., Feng, G., Homanics, Gregg E., . . . Zhang, F. (2015). Brains, Genes, and Primates. *Neuron, 86*(3), 617-631. doi:10.1016/j.neuron.2015.03.021

Benton, M. J., Donoghue, P. C. J., & Asher, R. J. (2009). *Calibrating and Constraining Molecular Clocks. In S. B. Hedges & S. Kumar (Eds.)* (1 ed.). New York: The Timetree of Life

Black, K. J., Koller, J. M., Snyder, A. Z., & Perlmutter, J. S. (2001). Template Images for Nonhuman Primate Neuroimaging: 2. Macaque. *NeuroImage, 14*(3), 744-748. doi:https://doi.org/10.1006/nimg.2001.0871

Black, K. J., Snyder, A. Z., Koller, J. M., Gado, M. H., & Perlmutter, J. S. (2001). Template Images for Nonhuman Primate Neuroimaging: 1. Baboon. *NeuroImage, 14*(3), 736-743. doi:https://doi.org/10.1006/nimg.2001.0752

Bohland, J. W., Wu, C., Barbas, H., Bokil, H., Bota, M., Breiter, H. C., . . . Mitra, P. P. (2009). A Proposal for a Coordinated Effort for the Determination of Brainwide Neuroanatomical Connectivity in Model Organisms at a Mesoscopic Scale. *PLOS Computational Biology, 5*(3), e1000334. doi:10.1371/journal.pcbi.1000334

Buckner, R. L., & Krienen, F. M. (2013). The evolution of distributed association networks in the human brain. *Trends in Cognitive Sciences, 17*(12), 648-665. doi:10.1016/j.tics.2013.09.017

Ceritoglu, C., Wang, L., Selemon, L. D., Csernansky, J. G., Miller, M. I., & Ratnanather, J. T. (2010). Large Deformation Diffeomorphic Metric Mapping Registration of Reconstructed 3D Histological Section Images and in vivo MR Images. *Furontiers in Human Neuroscience, 4*(43). doi:10.3389

Costa, M. S. M. O., R Santee, U., S Cavalcante, J., Moraes, P. R. A., P Santos, N., & Britto, L. R. G. (2000). *Retinohypothalamic projections in the common marmoset (Callithrix jacchus): A study using cholera toxin subunit B* (Vol. 415).

de la Mothe, L. A., Blumell, S., Kajikawa, Y., & Hackett, T. A. (2012). Thalamic Connections of Auditory Cortex in Marmoset Monkeys: Lateral Belt and Parabelt Regions. *The Anatomical Record: Advances in Integrative Anatomy and Evolutionary Biology, 295*(5), 822-836. doi:10.1002/ar.22454

Denk, W., & Horstmann, H. (2004). Serial Block-Face Scanning Electron Microscopy to Reconstruct Three-Dimensional Tissue Nanostructure. *PLOS Biology, 2*(11), e329. doi:10.1371/journal.pbio.0020329

Dooley, J., & Krubitzer, L. (2013). Cortical plasticity within and across lifetimes: how can development inform us about phenotypic transformations? *Frontiers in Human Neuroscience, 7*, 620.

dos Reis, M., Donoghue, P. C. J., & Yang, Z. (2014). Neither phylogenomic nor palaeontological data support a Palaeogene origin of placental mammals. *Biology Letters, 10*(1).

dos Reis, M., Inoue, J., Hasegawa, M., Asher, R. J., Donoghue, P. C. J., & Yang, Z. (2012). Phylogenomic datasets provide both precision and accuracy in estimating the timescale of placental mammal phylogeny. *Proceedings of the Royal Society B: Biological Sciences, 279*(1742), 3491.

Falchier, A., Clavagnier, S., Barone, P., & Kennedy, H. (2002). Anatomical Evidence of Multimodal Integration in Primate Striate Cortex. *The Journal of Neuroscience, 22*(13), 5749.

Felleman, D. J., & Essen, D. C. V. (1991). Distributed Hierarchical Processing in the Primate Cerebral Cortex. *Cerebral Cortex, 1*(1), 1-47.

Feng, L., Jeon, T., Yu, Q., Ouyang, M., Peng, Q., Mishra, V., . . . Huang, H. (2017). Population-averaged macaque brain atlas with high-resolution ex vivo DTI integrated into in vivo space. *Brain Structure and Function, 222*(9), 4131-4147. doi:10.1007/s00429-017-1463-6

Fujiyoshi, K., Hikishima, K., Nakahara, J., Tsuji, O., Hata, J., Konomi, T., . . . Okano, H. (2016). Application of q-Space Diffusion MRI for the Visualization of White Matter. *The Journal of Neuroscience, 36*(9), 2796.

Gallyas, F. (1979). Silever staining of myelin by means of physical development. *Neurol Res., 1*(2), 204-209.

Glaser, A. K., Chen, Y., Yin, C., Wei, L., Barner, L. A., Reder, N. P., & Liu, J. T. C. (2018). Multidirectional digital scanned light-sheet microscopy enables uniform fluorescence excitation and contrast-enhanced imaging. *Scientific Reports, 8*(1), 13878. doi:10.1038/s41598-018-32367-5

Grange, P., & Mitra, P. P. (2011). Algorithmic choice of coordinates for injections into the brain: encoding a neuroanatomical atlas on a grid. *eprint arXiv:1104.2616*.

Hashikawa, T., Nakatomi, R., & Iriki, A. (2015). Current models of the marmoset brain. *Neuroscience Research, 93*, 116-127.

Hennig, J., Nauerth, A., & Friedburg, H. (1986). RARE imaging: A fast imaging method for clinical MR. *Magnetic Resonance in Medicine, 3*(6), 823-833. doi:10.1002/mrm.1910030602

Hennig, J., Nauerth, A., & Friedburg, H. (1986). *RARE imaging: A fast imaging method for clinical MR* (Vol. 3).

Hikishima, K., Quallo, M. M., Komaki, Y., Yamada, M., Kawai, K., Momoshima, S., . . . Okano, H. (2011). Population-averaged standard template brain atlas for the common marmoset (Callithrix jacchus). *NeuroImage, 54*(4), 2741-2749. doi:https://doi.org/10.1016/j.neuroimage.2010.10.061

Hua, Y., Laserstein, P., & Helmstaedter, M. (2015). Large-volume en-bloc staining for electron microscopy-based connectomics. *Nature Communications, 6*, 7923. doi:10.1038/ncomms8923

Huo, B.-X., Zeater, N., Lin, M. K., Takahashi, Y. S., Hanada, M., Nagashima, J., . . . Mitra, P. P. (2018). Continuity between koniocellular layers of dorsal lateral geniculate and inferior pulvinar nuclei in common marmosets. *bioRxiv*, 315598. doi:10.1101/315598

ITK. (2017). ITK. Retrieved from https://itk.org/

1316 Janečka, J. E., Miller, W., Pringle, T. H., Wiens, F., Zitzmann, A., Helgen, K. M., . . .
1317   Murphy, W. J. (2007). Molecular and Genomic Data Identify the Closest Living
1318   Relative of Primates. *Science, 318*(5851), 792.
1319 Kakadu. (2016). The world's leading JPEG2000 software development toolkit.
1320   Retrieved from http://kakadusoftware.com/
1321 Kishi, N., Sato, K., Sasaki, E., & Okano, H. (2014). Common marmoset as a new model
1322   animal for neuroscience research and genome editing technology. *Development,*
1323   *Growth & Differentiation, 56*(1), 53-62.
1324 Kötter, R. (2004). Online retrieval, processing, and visualization of primate connectivity
1325   data from the CoCoMac Database. *Neuroinformatics, 2*(2), 127-144.
1326   doi:10.1385/NI:2:2:127
1327 Krubitzer, L., & Dooley, J. C. (2013). Cortical plasticity within and across lifetimes: how
1328   can development inform us about phenotypic transformations? *Frontiers in*
1329   *Human Neuroscience, 7*, 620. doi:10.3389/fnhum.2013.00620
1330 Krubitzer, L. A., & Seelke, A. M. H. (2012). Cortical evolution in mammals: The bane
1331   and beauty of phenotypic variability. *Proceedings of the National Academy of*
1332   *Sciences, 109*(Supplement 1), 10647.
1333 Leary, M. A., Bloch, J. I., Flynn, J. J., Gaudin, T. J., Giallombardo, A., Giannini, N. P., . .
1334   . Cirranello, A. L. (2013). The Placental Mammal Ancestor and the Post–K-Pg
1335   Radiation of Placentals. *Science, 339*(6120), 662.
1336 Lee, B. C., Lin, M. K., Fu, Y., Hata, J.-i., Miller, M. I., & Mitra, P. P. (2018). Joint Atlas-
1337   Mapping of Multiple Histological Series combined with Multimodal MRI of
1338   Whole Marmoset Brains and Quantification of Metric Distortions. *eprint*
1339   *arXiv:1805.04975*.
1340 Lin, M. K., Nicolini, O., Waxenegger, H., Galloway, G. J., Ullmann, J. F. P., & Janke, A.
1341   L. (2013). Interpretation of Medical Imaging Data with a Mobile Application: A
1342   Mobile Digital Imaging Processing Environment. *Frontiers in Neurology, 4*, 85.
1343   doi:10.3389/fneur.2013.00085
1344 Liu, J. V., Bock, N. A., & Silva, A. C. (2011). Rapid high-resolution three-dimensional
1345   mapping of T1 and age-dependent variations in the non-human primate brain
1346   using magnetization-prepared rapid gradient-echo (MPRAGE) sequence.
1347   *NeuroImage, 56*(3), 1154-1163.
1348   doi:https://doi.org/10.1016/j.neuroimage.2011.02.075
1349 Majka, P., Rosa, M. G. P., Bai, S., Chan, J. M., Huo, B.-X., Jermakow, N., . . . Mitra, P.
1350   P. (2018). Unidirectional monosynaptic connections from auditory areas to the
1351   primary visual cortex in the marmoset monkey. *Brain Structure and Function*.
1352   doi:10.1007/s00429-018-1764-4
1353 Mansfield, P., & Pykett, I. L. (1978). Biological and medical imaging by NMR. *Journal*
1354   *of Magnetic Resonance (1969), 29*(2), 355-373. doi:https://doi.org/10.1016/0022-
1355   2364(78)90159-2
1356 Markov, N. T., Ercsey-Ravasz, M. M., Ribeiro Gomes, A. R., Lamy, C., Magrou, L.,
1357   Vezoli, J., . . . Kennedy, H. (2014). A Weighted and Directed Interareal
1358   Connectivity Matrix for Macaque Cerebral Cortex. *Cerebral Cortex, 24*(1), 17-36.
1359   doi:10.1093/cercor/bhs270
1360 Markov, N. T., Misery, P., Falchier, A., Lamy, C., Vezoli, J., Quilodran, R., . . .
1361   Knoblauch, K. (2011). Weight Consistency Specifies Regularities of Macaque

Cortical Networks. *Cerebral Cortex, 21*(6), 1254-1272. doi:10.1093/cercor/bhq201

Marx, V. (2016). Neurobiology: learning from marmosets. *Nature Methods, 13*, 911. doi:10.1038/nmeth.4036

Mayerich, D., Abbott, L., & McCormick, B. (2008). Knife-edge scanning microscopy for imaging and reconstruction of three-dimensional anatomical structures of the mouse brain. *Journal of Microscopy, 231*(1), 134-143. doi:10.1111/j.1365-2818.2008.02024.x

Miller, Cory T., Freiwald, Winrich A., Leopold, David A., Mitchell, Jude F., Silva, Afonso C., & Wang, X. (2016). Marmosets: A Neuroscientific Model of Human Social Behavior. *Neuron, 90*(2), 219-233. doi:10.1016/j.neuron.2016.03.018

Mitchell, J. F., & Leopold, D. A. (2015). The marmoset monkey as a model for visual neuroscience. *Neuroscience Research, 93*(Supplement C), 20-46. doi:10.1016/j.neures.2015.01.008

Mitra, P. P. (2014). The Circuit Architecture of Whole Brains at the Mesoscopic Scale. *Neuron, 83*(6), 1273-1283. doi:10.1016/j.neuron.2014.08.055

Modha, D. S., & Singh, R. (2010). Network architecture of the long-distance pathways in the macaque brain. *Proceedings of the National Academy of Sciences, 107*(30), 13485.

Mundinano, I.-C., Flecknell, P. A., & Bourne, J. A. (2016). MRI-guided stereotaxic brain surgery in the infant and adult common marmoset. *Nature Protocols, 11*, 1299. doi:10.1038/nprot.2016.076 https://www.nature.com/articles/nprot.2016.076 - supplementary-information

NIfTI-1 Data Format. (2016). Neuroimaging Informatics Technology Initiative. Retrieved from nifti.nimh.nih.gov/nifti-1

Nikon. (2018). Light Sheet Fluorescence Microscopy Retrieved from https://www.microscopyu.com/techniques/light-sheet/light-sheet-fluorescence-microscopy

Nissl, F. (1894). Ueber eine neue Untersuchungsmethode des Centralorgans zur Feststellung der Localisation der Nervenzellen. . *Neurologisches Centralblatt., 13*, 507-508.

Oh, S. W., Harris, J. A., Ng, L., Winslow, B., Cain, N., Mihalas, S., . . . Zeng, H. (2014). A mesoscale connectome of the mouse brain. *Nature, 508*(7495), 207-214. doi:10.1038

Okano, H., & Kishi, N. (2018). Investigation of brain science and neurological/psychiatric disorders using genetically modified non-human primates. *Current Opinion in Neurobiology, 50*, 1-6. doi:10.1016/j.conb.2017.10.016

Okano, H., & Mitra, P. (2015). Brain-mapping projects using the common marmoset. *Neuroscience Research, 93*, 3-7.

Okano, H., Sasaki, E., Yamamori, T., Iriki, A., Shimogori, T., Yamaguchi, Y., . . . Miyawaki, A. (2015). Brain/MINDS: A Japanese National Brain Project for Marmoset Neuroscience. *Neuron, 92*(3), 582-590. doi:10.1016/j.neuron.2016.10.018

Osten, P., & Margrie, T. W. (2013). Mapping brain circuitry with a light microscope. *Nature Methods, 10*, 515. doi:10.1038/nmeth.2477

Pahariya, G., Das, S., Jayakumar, J., Bannerjee, S., Vangala, V., Ram, K., & Mitra, P. P. (2018). High precision automated detection of labeled nuclei in terabyte-scale whole-brain volumetric image data of mouse. *bioRxiv*.

Park, J. E., Zhang, X. F., Choi, S.-H., Okahara, J., Sasaki, E., & Silva, A. C. (2016). Generation of transgenic marmosets expressing genetically encoded calcium indicators. *Scientific Reports, 6*, 34931. doi:10.1038/srep34931

Paxinos, G., Watson, C., Petrides, M., Rosa, M., & Tokuno, H. (2012). *The Marmoset Brain in Stereotaxic Coordinates* (1st ed.). United States: Academic Press.

Pilati, N., Barker, M., Panteleimonitis, S., Donga, R., & Hamann, M. (2008). A rapid method combining Golgi and Nissl staining to study neuronal morphology and cytoarchitecture. . *Journal Histochem Cytochem., 56*, 539-550.

Pinskiy, V., Jones, J., Tolpygo, A. S., Franciotti, N., Weber, K., & Mitra, P. P. (2015). High-Throughput Method of Whole-Brain Sectioning, Using the Tape-Transfer Technique. *PLOS ONE, 10*(7). doi:10.1371

Pinskiy, V., Tolpygo, A. S., Jones, J., Weber, K., Franciotti, N., & Mitra, P. P. (2013). A low-cost technique to cryo-protect and freeze rodent brains, precisely aligned to stereotaxic coordinates for whole-brain cryosectioning. *Journal of Neuroscience Methods, 218*, 206-213.

Piotr, M., Tristan, A. C., Hsin-Hao, Y., Alexander, T., Partha, P. M., Daniel, K. W., & Marcello, G. P. R. (2016). Towards a comprehensive atlas of cortical connections in a primate brain: Mapping tracer injection studies of the common marmoset into a reference digital template. *524, 11*, 2161-2181. doi:10.1002/cne.24023

Quallo, M. M., Price, C. J., Ueno, K., Asamizuya, T., Cheng, K., Lemon, R. N., & Iriki, A. (2010). Creating a population-averaged standard brain template for Japanese macaques (M. fuscata). *NeuroImage, 52*(4), 1328-1333. doi:https://doi.org/10.1016/j.neuroimage.2010.05.006

Raspberry Pi. (2016). Raspberry Pi Foundation. Retrieved from https://www.raspberrypi.org/

Reser, D. H., Burman, K. J., Richardson, K. E., Spitzer, M. W., & Rosa, M. G. P. (2009). Connections of the marmoset rostrotemporal auditory area: express pathways for analysis of affective content in hearing. *European Journal of Neuroscience, 30*, 578-592.

Reser, D. H., Burman, K. J., Yu, H.-H., Chaplin, T. A., Richardson, K. E., Worthy, K. H., & Rosa, M. G. P. (2013). Contrasting Patterns of Cortical Input to Architectural Subdivisions of the Area 8 Complex: A Retrograde Tracing Study in Marmoset Monkeys. *Cereb Cortex, 23*(8). doi:10.1093

Reser, D. H., Majka, P., Snell, S., Chan, J. M. H., Watkins, K., Worthy, K., . . . Rosa, M. G. P. (2017). Topography of Claustrum and Insula Projections to Medial Prefrontal and Anterior Cingulate Cortices of the Common Marmoset (Callithrix jacchus). *Journal of Comparative Neurology, 525*(6), 1421-1441. doi:10.1002/cne.24009

Sasaki, E., Suemizu, H., Shimada, A., Hanazawa, K., Oiwa, R., Kamioka, M., Tomioka, I., Sotomaru, Y., Hirakawa, R., Eto, T., Shiozawa, S., Maeda, T., Ito, M., Ito, R., Kito, C., Yagihashi, C., Kawai, K., Miyoshi, H., Tanioka, Y., Tamaoki, N., Habu, S., Okano, H., Nomura, T.,. (2009). Generation of transgenic non-human primates with germline transmission. *Nature, 459*, 523–527.

Sato, K., Oiwa, R., Kumita, W., Henry, R., Sakuma, T., Ito, R., . . . Sasaki, E. (2016). Generation of a Nonhuman Primate Model of Severe Combined Immunodeficiency Using Highly Efficient Genome Editing. *Cell Stem Cell, 19*(1), 127-138. doi:10.1016/j.stem.2016.06.003

Solomon, S. G., & Rosa, M. G. P. (2014). A simpler primate brain: the visual system of the marmoset monkey. *Frontiers in Neural Circuits, 8*, 96. doi:10.3389/fncir.2014.00096

Springer, M. S., Meredith, R. W., Janecka, J. E., & Murphy, W. J. (2011). The historical biogeography of Mammalia. *Philosophical Transactions of the Royal Society B: Biological Sciences, 366*(1577), 2478.

Stephan, K. E. (2013). The history of CoCoMac. *NeuroImage, 80*(Supplement C), 46-52. doi:10.1016/j.neuroimage.2013.03.016

Stephan, K. E., Kamper, L., Bozkurt, A., Burns, G. A. P. C., Young, M. P., & Kötter, R. (2001). Advanced database methodology for the Collation of Connectivity data on the Macaque brain (CoCoMac). *Philosophical Transactions of the Royal Society of London. Series B: Biological Sciences, 356*(1412), 1159.

Svoboda, K., & Yasuda, R. (2006). Principles of Two-Photon Excitation Microscopy and Its Applications to Neuroscience. *Neuron, 50*(6), 823-839. doi:https://doi.org/10.1016/j.neuron.2006.05.019

Takai, M. (2002). Evolution of early hominids : recent fossil records and phylogenetic hypotheses. *The Palaeontological Society of Japan (PSJ), 71*, 29-43.

Wilkinson, R. D., Steiper, M. E., Soligo, C., Martin, R. D., Yang, Z., & Tavaré, S. (2011). Dating Primate Divergences through an Integrated Analysis of Palaeontological and Molecular Data. *Systematic Biology, 60*(1), 16-31. doi:10.1093/sysbio/syq054

William, D. P., Karl, J. F., John, T. A., Stefan, J. K., & Thomas, E. N. (2011). *Statistical Parametric Mapping: The Analysis of Functional Brain Images* (1 ed.): Academic Press.

Woodward, A., Hashikawa, T., Maeda, M., Kaneko, T., Hikishima, K., Iriki, A., . . . Yamaguchi, Y. (2017). The Brain/MINDS 3D digital marmoset brain atlas. *bioRxiv*.

Yeh, F.-C., Panesar, S., Fernandes, D., Meola, A., Yoshino, M., Fernandez-Miranda, J. C., . . . Verstynen, T. (2018). Population-averaged atlas of the macroscale human structural connectome and its network topology. *NeuroImage, 178*, 57-68. doi:https://doi.org/10.1016/j.neuroimage.2018.05.027

Zingg, B., Hintiryan, H., Gou, L., Song, Monica Y., Bay, M., Bienkowski, Michael S., . . . Dong, H.-W. (2014). Neural Networks of the Mouse Neocortex. *Cell, 156*(5), 1096-1111. doi:https://doi.org/10.1016/j.cell.2014.02.023

Supplementary Figures
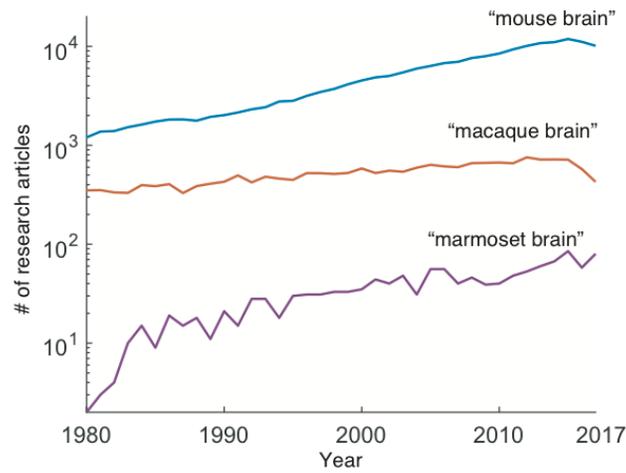
Figure 1-figure supplement 1. **Marmoset brain research articles increase 1980-2017 compared with mouse and macaque brain research listed on PubMed (www.ncbi.nlm.nih.gov/pubmed)**. Number of articles are plotted in logarithmic scale for results returned from searching the keywords of 'mouse brain', 'macaque brain', or 'marmoset brain'.
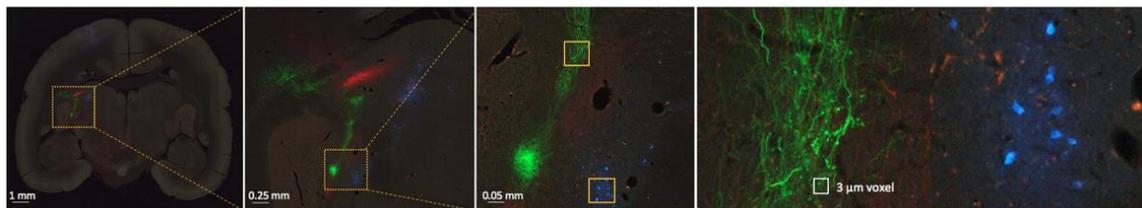
Figure 2-figure supplement 1. **Example of a coronal section of the brain showing fluorescent tracers in high magnification.** We have obtained each coronal section in 0.46μm per pixel with 20 μm section thickness. The mesoscale level image (high magnification on the right) shows clear projections in the thalamus with labeled cells/axons in representative subcortical regions.

Video 1

1511

1512 Video 1: **The registration process permitted brain surface reconstruction**. A brain fully reconstructed using MRI

1513 guided registration with process and cell detection. A clear pathway is seen from the tracer traveling from region to region

1514 in this 3d visualization of projections. Virtual cuts in planes of sections other than the original coronal sections are also

1515 shown.

Supplementary File 1

1516

1517 File 1: List of target structures and number of injections.

Supplementary File 2

1518

1519 File 2: Reference list of trace tracing studies.